Measuring Ocean Total Surface Current Velocity with the KuROS and KaRADOC airborne near-nadir Doppler radars: a multi-scale analysis in preparation of the SKIM mission

Louis Marié[1], Fabrice Collard[2], Frédéric Nouguier[1], Lucia Pineau-Guillou[1], Danièle Hauser[3], François Boy[4], Stéphane Méric[5], Peter Sutherland[1], Charles Peureux[1], Goulven Monnier[6], Bertrand Chapron[1], Adrien Martin[7], Pierre Dubois[8], Craig Donlon[9], Tania Casal[9], and Fabrice Ardhuin[1]

[1]Laboratoire d'Océanographie Physique et Spatiale (LOPS), UMR 6523, Univ. Brest, CNRS, Ifremer, IRD, Brest, France
[2]OceanDataLab, Locmaria Plouzané, France
[3]CNRS, Univ. Versailles St Quentin, Sorbonne Université, LATMOS, France
[4]CNES, Toulouse, France
[5]Institut d'Électronique et de Télécommunication de Rennes (IETR), UMR CNRS 6164, Rennes, France
[6]SCALIAN, Rennes, France
[7]NOC, Southampton, UK
[8]CLS, Ramonville St Agne, France
[9]ESA, Nordwijk, The Netherlands

Correspondence to: Fabrice Ardhuin (fabrice.ardhuin@univ-brest.fr)

Abstract. Surface currents are poorly known over most of the world's oceans. Satellite-borne Doppler Waves and Current Scatterometers (DWaCS) are one of the proposed techniques to fill this observation gap. The Sea surface KInematics Multiscale (SKIM) proposal is the first satellite concept built on a DWaCS design at near-nadir angles, and was demonstrated to be technically feasible as part of the European Space Agency Earth Explorer program. This article describes preliminary results from a field experiment performed in November 2018 off the French Atlantic coast, with sea states representative of the open ocean and a well known tide-dominated current regime, as part of the detailed design and feasibility studies for SKIM. This experiment comprised airborne measurements performed using Ku-band and Ka-band Doppler radars looking at the sea surface at near-nadir incidence in a real-aperture mode, i.e. in a geometry and mode similar to that of SKIM, as well as an extensive set of in-situ instruments. The KuROS airborne radar provided simultaneous measurements of the radar backscatter and Doppler velocity, in a side-looking configuration, with a horizontal resolution of about 5 to 10 m along the line of sight and integrated in the perpendicular direction over the real-aperture 3-dB footprint diameter (about 580 m). The KaRADOC system, also operating in the side-looking configuration, had a much narrower beam, with a circular footprint only 45 m in diameter. Results are reported for two days with contrasting conditions, a strong breeze on 2018/11/22 (wind speed 11.5 m.s^{-1}, Hs 2.6 m), and gentle breeze on 2018/11/24 (wind speed 5.5 m.s^{-1}, Hs 1.7 m). The measured line-of-sight velocity signal is analysed to separate a non-geophysical contribution, linked to the aircraft velocity, a geophysical contribution due to the intrinsic motion of surface waves, and the desired surface current contribution. The surface waves contribution is found to be well predicted by Kirchhoff scattering theory using as input parameters in-situ measurements of the directional spectrum of long waves, complemented by the short-waves spectrum of (Elfouhaily et al., 1997). It is found to be closely aligned with

the wind direction, with small corrections due to the presence of swell. Its norm is found to be weakly variable with wind speed and sea state, quite stable and close to $C_0 = 2.0\,\mathrm{m.s}^{-1}$ at Ka-band, more variable and close to $C_0 = 2.4\,\mathrm{m.s}^{-1}$ at Ku-band. These values are 10-20% smaller than previous theoretical estimates. The directional spread of the short gravity waves is found to have a marked influence on this surface waves contribution. Overall, the results of this study support the feasibility of near-nadir radar Doppler remote sensing of the ocean TSCV.

1 Introduction

The ocean Total Surface Current Velocity (TSCV) is defined as the Lagrangian mean velocity at the instantaneous sea surface, corresponding to an effective mass transport velocity at the surface. The TSCV is currently only reliably measured by High-Frequency (HF) radars, deployed in some coastal regions. Elsewhere, available estimates depend on numerical model outputs, sea level and wind measurements, and on assumptions such as balance between surface pressure gradient and the Coriolis force. The situation is similar regarding Directional wave statistics, which are currently mainly estimated through numerical modeling.

These estimates of the TSCV are not reliable at small scales, particularly so in the tropical ocean (e.g. Sudre et al., 2013; Stopa et al., 2016), and these limitations hamper current efforts to observe and understand the fluxes of heat, freshwater, carbon, plastics, and the coastal impacts of sea states.

Whereas new data on ocean waves are becoming available with the Surface Waves Investigation and Monitoring (SWIM) instrument carried by the China France Ocean SATellite (CFOSAT) (Hauser et al., 2017; Hauser et al., 2020), direct spaceborne measurements of surface current have been limited to a few regions and single projections of the current vector (Chapron et al., 2005; Rouault et al., 2010; Hansen et al., 2011). Several concepts based on SAR interferometry (Romeiser et al., 2003; Buck, 2005) or Doppler scatterometry (Rodriguez, 2018; Chelton et al., 2019) have been proposed for satellite missions aimed at mapping the ocean surface current vector (see review by Ardhuin et al., 2019). Airborne demonstrators have also been developed in that context (Martin et al., 2018; Rodríguez et al., 2018), and are now becoming operational tools for oceanographic research.

The Doppler frequency shift (DFS) signal provided by these phase-resolving radar instruments is complex: it contains a geophysical contribution due to waves and currents, as well as a large non-geophysical contribution due to the platform motion. The platform velocity in space being of the order of 7 km/s for low Earth orbit, it is obviously critical to have an accurate knowledge of the measurement geometry to correctly estimate the non-geophysical component. The contribution due to ocean waves is however also an order of magnitude larger than the expected TSCV contribution (Nouguier et al., 2018), and must also be precisely estimated, using an accurate sea state description.

The Sea surface KInematics Multiscale monitoring (SKIM) satellite mission has been designed to address all these requirements and provide direct global-coverage measurements of TSCV. It is based on the combination of two instruments, the SKIM Ka-band Radar (SKaR), a phase-resolved SWIM-like conically scanning radar, providing simultaneous Ka-band observations of sea state and DFS, and a state-of-the-art nadir altimeter, providing the sea surface elevation observations necessary to control the SKaR acquisition geometry with sufficient accuracy, but also significant wave height and wind speed observations.

SKIM was pre-selected as one of the two candidate missions for the European Space Agency (ESA) 9th Earth Explorer. As part of the detailed design and feasibility (phase A) studies, ESA funded a dedicated measurements campaign, Drift4SKIM, which was organized from November 21st to 27th, 2018, off the French Atlantic coast, in an area with sea states characteristic of the open ocean and a well known tide-dominated current regime, monitored by a two-sites 12 MHz High-Frequency radar system (Ardhuin et al., 2009). A range of in-situ instruments (surface current drifters, drifting and moored wave-measuring buoys), as well as two airborne Doppler radars operating in the Ku- (KuROS) and Ka- (KaRADOC) bands, were deployed. The campaign goals were to:

- Demonstrate how the non-geophysical contribution V_{NG} to the DFS can be estimated from the motion of the platform carrying the radar, the antenna diagram properties and the azimuth and incidence-angle dependencies of the radar cross section.

- Explore the geophysical component V_{GD} and its decomposition as a sum of contributions due to currents and waves, V_{CD} and V_{WD} (Nouguier et al., 2018).

- Validate the Radar Sensing Satellite Simulator (Nouguier, 2019) and its capability to simulate airborne configurations.

As highlighted in Figure 1, the viewing geometry of an airborne system is vastly different from that of a satellite system, with a much smaller footprint and incidence angle variations at scales comparable to the wavelength of the dominant ocean waves. Another obvious difference is the stability of the platform and its velocity, 7 km/s for low Earth orbit, and around 120 m/s for the ATR-42 aircraft used here. As a result, transposing the performance of an airborne system to a satellite system requires a thorough analysis, supplemented by carefully designed and validated simulation tools. Performing this analysis is however worthwhile, as it leads one to develop valuable insight into the instrument imaging principle and design trade-offs.

This article is intended to provide an overview of the Drift4SKIM campaign data and a first discussion of their implications for the emerging field of near-nadir Doppler radar observations of TSCV. It is structured as follows: the principle of the pulse-pair measurements and the different contributions to the observed DFS are detailed in section 2 and Appendix A. Section 3 gives a brief account of the field work performed and conditions encountered during the campaign. The results of the airborne measurements are exposed in section 4. Results and implications for SKIM are then discussed in section 5. Conclusions and perspectives follow in section 6.
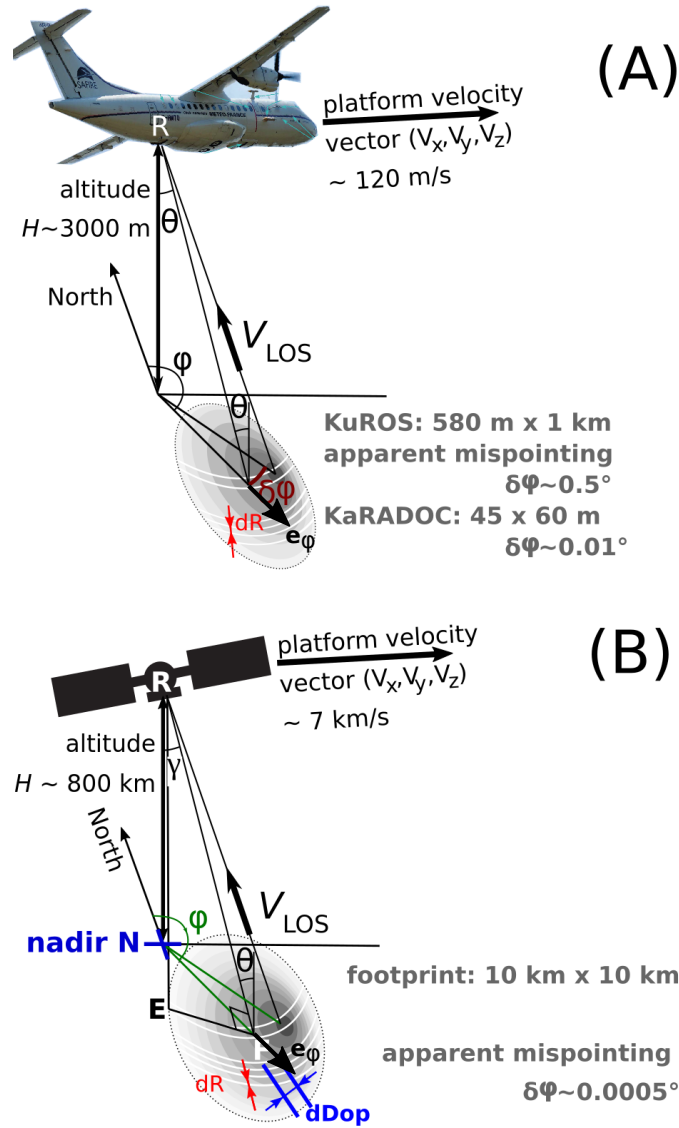
Figure 1. (A) Schematic of ATR-42 and KuROS instrument and definition of viewing angles, azimuth φ and incidence angle θ, and (B) comparison with the SKIM viewing geometry. The unit vector $\mathbf{e}_\varphi$ is the projection on the horizontal of the line of sight direction vector. The variation of surface backscatter across the footprint and as a function of azimuth φ, which causes the effective mispointing $\delta\varphi$, is represented as a grey shading. In the KuROS data, each measurement is integrated in azimuth across the antenna lobe. In the case of SKIM, the use of unfocused SAR processing allows the separation of echoes in the azimuth direction with a resolution dDop$\simeq 300$ m.

2 Near-nadir radar Doppler measurements of ocean velocities: theory

Ship-borne Doppler measurements of ocean currents are routinely performed using so-called "Vessel-Mounted Acoustic Doppler Current Profilers" (VMADCPs, see for instance Rossby et al., 2019). Some of the data processing concepts transpose directly to the space-borne context: the raw DFS signal contains a large non-geophysical contribution due to the platform motion, which must be estimated from ancillary sensors and compensated. The accuracy of the final geophysical product is practically set by the accuracy of the non-geophysical velocity estimation and correction procedure. In the VMADCP context, however, the backscattering elements responsible for the production of the acoustic return signal (particulate suspended matter, zooplanktonic organisms) are passive and follow accurately the water mass. This does not carry over in the electromagnetic case: here, the return signal is produced by the interaction of the transmitted signal with the roughness elements of the sea surface, which move with respect to the water mass with an intrinsic phase velocity that is an order of magnitude larger than typical ocean currents. This effect is for instance well known in the ground-based HF-radar currents measurement context (Stewart and Joy, 1974), and must also be compensated.

In our case, the measurement geometry is represented in figure 1, and the line-of-sight Doppler velocity V_{LOS} looking towards incidence angle θ and azimuth φ (in this paper, line-of-sight DV contributions are denoted by "V", and the corresponding horizontal velocity contributions are denoted by "U") is the sum of the projection of a horizontal current contribution $U_{\text{CD}}(\varphi)$, a wave-induced contribution $V_{\text{WD}}(\theta, \varphi)$ and a non-geophysical contribution $V_{\text{NG}}(\theta, \varphi)$. The equation that permits the retrieval of the TSCV contribution $U_{\text{CD}}(\varphi)$ from the raw measured V_{LOS} can be written as

$$U_{\text{CD}}(\varphi) = \frac{[V_{\text{LOS}}(\theta, \varphi) - V_{\text{NG}}(\theta, \varphi) - V_{\text{WD}}(\theta, \varphi)]}{\sin \theta}. \tag{1}$$

The aim of this section is to provide a detailed analysis of the different terms of this expression. The non-geophysical contribution V_{NG} is discussed in subsection 2.1 and Appendix A. The wave Doppler contribution is discussed in subsection 2.2. A brief summary of the measurement error budget is finally provided in subsection 2.3.

2.1 Non-geophysical velocity V_{NG}

As mentioned above, the accuracy of ship-borne acoustic Doppler current measurements is affected in a dominant way by the platform motion compensation process. In the space-borne context, the platform velocity is almost three orders of magnitude larger ($7000\,\text{m.s}^{-1}$ *vs.* $10\,\text{m.s}^{-1}$). The accuracy requirements are thus tremendously exacerbated, and attention must in particular be paid to the detailed effects of the antenna radiation diagram and sea-surface Normalized Radar Cross Section (NRCS) variations with space and observation azimuth. A detailed discussion of these effects is given in Appendix A.

In summary, in the case of a sufficiently narrow radiation diagram, V_{NG} can be approximated as the radar carrier velocity projected on an effective look direction. This effective look direction differs from the geometric boresight direction by an effective azimuthal mispointing $\delta\varphi$ due to the finite antenna beamwidth combined with the variations of NRCS within the radar footprint, and by an effective incidence angle mispointing $\delta\theta$ due to radar timing or surface-tracking errors.

The beamwidth at the working incidence angle is thus a very important parameter of a radar intended for TSCV measurements. Table 1 summarizes the parameters of the KuROS and KaRADOC antennas. For KuROS they have been determined

Table 1. KuROS and KaRADOC antenna radiation diagrams characteristics. All angles are in degrees. See Appendix B for the definitions of α and β

Instrument	KuROS	KaRADOC
Polarization	HH	HH
Azimuth 1-way beamwidth ($\alpha_{-3\text{dB}}$)	15.0	1.85
Elevation 1-way beamwidth ($\beta_{-3\text{dB}}$)	22.6	1.20
Boresight elevation (β^0)	11.8	12.1
Boresight azimuth (deg)	~ 0	-0.05

following the procedure detailed in Appendix B. For KaRADOC, they are the result of anechoic chamber measurements (Appendix C). As discussed in Appendix B, these parameters describe the antenna radiation diagrams when expressed as functions of variables, α and β, which do not coincide with azimuth and incidence angle. In the case of constant altitude flight and near-nadir observations with the antenna looking towards azimuth φ_b, one can however obtain a Gaussian approximation to the 1-way radiation diagram as:

$$G \simeq \exp\left[-\frac{(\varphi - \varphi_b)^2}{2}\left[\frac{\sin^2(\theta)}{\sigma_\alpha^2} + \frac{(\beta_0 - \tan(\theta))\tan(\theta)}{\sigma_\beta^2} \right] \right], \tag{2}$$

where $\sigma_\alpha = \alpha_{-3\text{dB}}/\sqrt{8\log(2)}$ and $\sigma_\beta = \beta_{-3\text{dB}}/\sqrt{8\log(2)}$. For 12° observations the second term in the exponential can safely be neglected, and the effective azimuthal beamwidth can be estimated as:

$$\varphi_{-3\text{dB}} = \frac{\alpha_{-3\text{dB}}}{\sin(\theta)}. \tag{3}$$

When projected on the ground, $\varphi_{-3\text{dB}}$ is thus larger than $\alpha_{-3\text{dB}}$ by a factor $1/\sin(\theta)$, equal to 4.8 for 12° measurements. Provided that the beam is not too wide, the Gaussian approximation eq. (A29) of G as a function of φ can then be used, with parameter

$$\sigma_\varphi \simeq \alpha_{-3\text{dB}} / \left[\sin\theta \sqrt{8\log(2)} \right]. \tag{4}$$

Due to the width of the azimuthal aperture, the NRCS-weighted line-of-sight azimuth φ_a can differ from the boresight azimuth φ_b by a mispointing angle $\delta\varphi$. Expressions for $\delta\varphi$ are obtained in Appendix A in the two limiting cases of slow linear and fast sinusoidal variations of the ocean surface NRCS with respect to azimuth. In the slow variation case, $\delta\varphi$ is obtained as

$$\delta\varphi = \varphi_a - \varphi_b = \frac{1}{2}\frac{\sigma_\alpha^2}{\sin^2\theta}\frac{1}{\sigma^0}\frac{\partial\sigma^0}{\partial\varphi}. \tag{5}$$

Denoting by φ_t the flight track azimuth and V_p the along-track flight velocity, the spurious "Azimuth Gradient Doppler" contribution to the DV caused by the mispointing reads

$$U_{\text{AGD}} = \sin(\varphi_b - \varphi_t)\frac{V_p}{2}\frac{\sigma_\alpha^2}{\sin^2\theta}\frac{1}{\sigma^0}\frac{\partial\sigma^0}{\partial\varphi}. \tag{6}$$
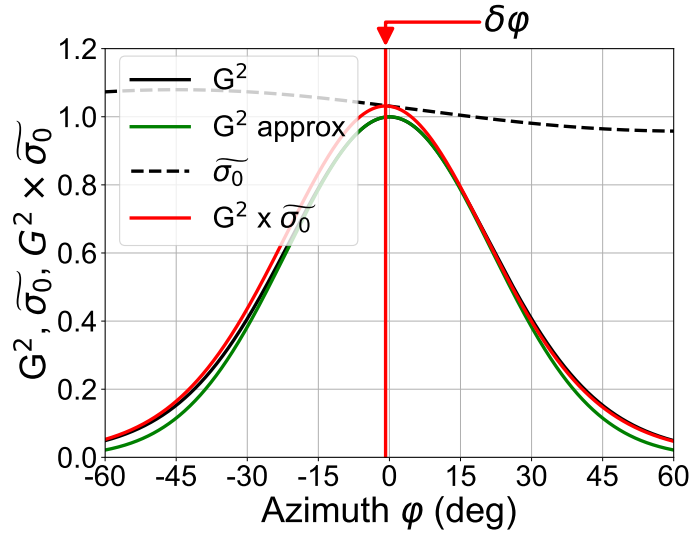
Figure 2. KuROS azimuth integral weight at $\theta = 12°$ for a north-facing ($\varphi_b = 0°$) antenna (black), Gaussian approximation (eq. A29) (green) and variation of $\widetilde{\sigma^0}$ for a typical 11 m.s^{-1} wind from 140° (dashed black). The peak of the $\widetilde{\sigma^0} \, G^2$ product (red) is shifted with respect to the peak of G^2 by $\delta\varphi \simeq -0.81°$.

As an example, figure 2 shows the variations of the two-way antenna radiation diagram G^2, of its Gaussian approximation, and of the $G^2\widetilde{\sigma^0}$ (see eq. A11) product as a function of azimuth at 12° incidence angle, for a northward-looking KuROS antenna ($\varphi_b = 0°$), using σ^0 data from the Drift4SKIM campaign on 2018/11/22. The effect of the wind-induced azimuthal gradient of σ^0 is to shift the effective radiation diagram towards the brighter upwind/downwind directions, with an apparent pointing azimuth φ_a. The shift induced in this case is $\delta\varphi = \varphi_a - \varphi_b = -0.81° = -15 \times 10^{-3}$ rad. For comparison (see section 2.3 and table 2), the pointing accuracy required to achieve a 15 cm/s error on the horizontal current in the airborne configuration is 1.2 milliradians.

Here, it is important to note that KuROS was not specifically designed for this experiment, but primarily as a Calibration/Validation instrument for the CFOSAT mission, which required a broad radiation diagram. Though the analysis of the KuROS data helped uncover many interesting effects relevant to Doppler observations of the sea surface, its design was not fully appropriate to validate the inversion of the geophysical velocities, for which the pencil-beam antenna diagram of KaRADOC was better suited.

Figure 3.A shows a typical example of the azimuthal variation of $\widetilde{\sigma^0}$ at 12° incidence angle for Ku-band. As expected for near-nadir measurements (Chapron et al., 2002; Munk, 2008; Chu et al., 2012), the NRCS is largest in the downwind look direction ($\varphi = 320°$), has a secondary peak in the upwind direction, and is weakest in the crosswind look directions. Figure 3.B shows the corresponding U_{AGD} contribution for the KuROS and KaRADOC cases, using an aircraft velocity $V_p = 120$
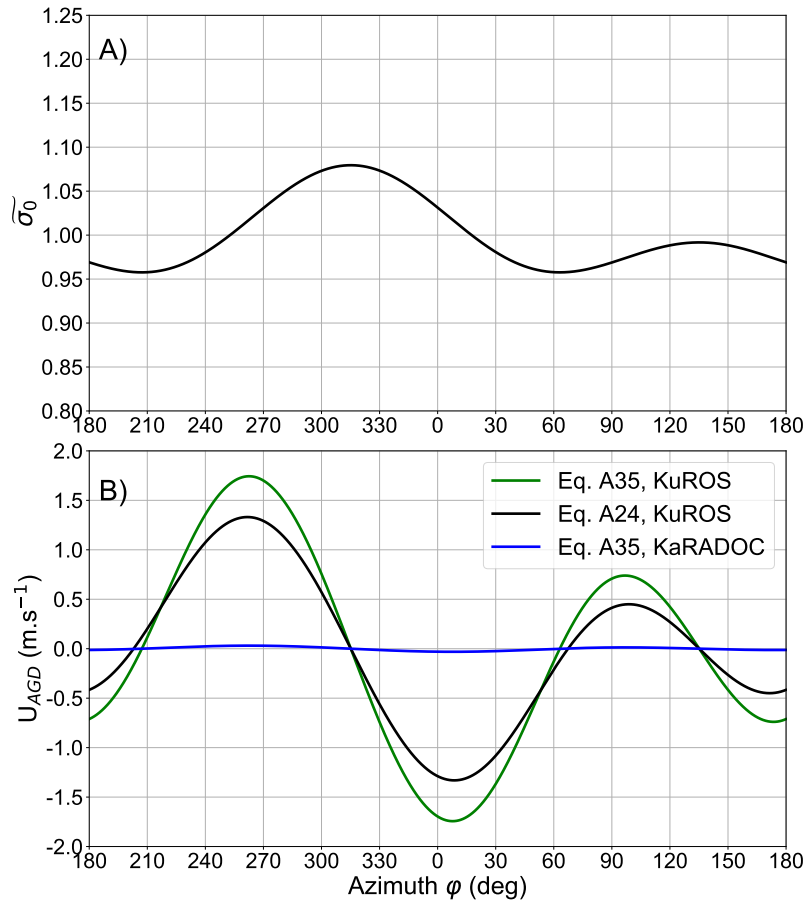
Figure 3. A) Example of azimuthal variation of $\widetilde{\sigma^0}$ at 12° incidence angle, corresponding to the November 22nd case (11 m/s wind from 140°) discussed in section 3, and B) associated spurious velocity U_{AGD} as a function of look azimuth φ_b in the case of a port-looking antenna mounted on a platform in constant altitude flight at 120 m/s. For the KuROS case, the green line shows the result of the approximate eq. (A35) and the black line shows the result of the full azimuthal integration eq. (A24). The blue line represents the result of eq. (A35) for KaRADOC, using the same $\widetilde{\sigma^0}$ as in the Ku-band case.

m s^{-1} and the Ku-band NRCS fit for both instruments (this is a reasonable assumption for order-of-magnitude estimates). As detailed in Appendix A, equations (5) and (6) only apply for a narrow beam when projected on the ground, which is not a very good approximation for the KuROS case, even at 12° incidence angle. As shown in figure 2, the Gaussian approximation for the antenna diagram as a function of φ gives a too narrow distribution and does not take properly into account the azimuthal integration, leading to an overestimation of U_{AGD}. It is clear however that even the more exact equation A24 gives very large correction magnitudes, in excess of $1.2\ \mathrm{m.s}^{-1}$ in some azimuth ranges.

Because the azimuth gradient U_{AGD} contribution to the observed DV is proportional to $V_p\sigma_\varphi^2$, this effect is much larger (and correcting it is correspondingly more demanding in terms of antenna characterization) for KuROS, than for KaRADOC or

DopplerScatt (Rodríguez et al., 2018), thanks to their narrow azimuthal beam aperture. Another remark is that the approximate expression eq. (A35), though it gives the appropriate dependency of U_{AGD} with respect to look azimuth, tends to over-predict its magnitude, as the widening associated to the ground projection saturates for broad beams.

Although the relative variations $\partial_\varphi \sigma^0 / \sigma^0$ are larger for larger incidence angles, this is more than compensated by the $1/\sin^2\theta$ reduction in azimuthal diversity across the footprint. This effect can thus be neglected for much higher incidence angles (Rodríguez et al., 2018).

2.2 Geophysical velocity U_{GD}: Waves and Current Doppler velocities

The geophysical part of the DFS measured by a microwave radar over the ocean, using both Along-Track-Interferometry and Doppler centroid techniques emerges from the average over the instrument field of view (FOV) of the backscatter-weighted line of sight projection of the surface velocity, as illustrated in figure 4.

In the well-understood case of decametric electromagnetic waves interacting with the sea surface at grazing incidence, the interaction is dominated by the Bragg coherent backscattering mechanism (Crombie, 1955), in which the backscattered field reflects the properties (amplitude, phase speed) of a very finely selected component of the sea state, namely that whose wavevector is precisely equal to the so-called Ewald vector, the difference between the wavectors of the scattered and incident electromagnetic waves. Exploiting the deviation of the phase speed of this sea state component from its theoretical value is the principle of the HF radars operationally used to measure the ocean TSCV in coastal areas (Barrick et al., 1974; Stewart and Joy, 1974).

In the case of the near-nadir interaction of microwaves with the sea surface, which is the configuration considered for SKIM and used by the AirSWOT, KuROS and KaRADOC airborne instruments, this mental picture must be adapted: the Bragg scattering mechanism is not dominant, and the main contribution comes from quasi-specular reflections on those facets of the sea surface which are normal to the Ewald vector. The backscattering cross-section of the sea surface and DFS in this case do not depend on the properties of a single Fourier component of the sea state, but on the probability density function of the sea surface slope, which is a complex functional of its entire directional spectrum.

As discussed by (Nouguier et al., 2018), who applied it to the analysis of AirSWOT NRCS and DFS data collected during the Gulf of Mexico LASER experiment of 2016, the theoretical framework appropriate to this configuration is the Kirchhoff Approximation (Beckmann and Spizzichino, 1987). In this approximation, the geophysical DFS ω_{GD} can be expressed as:

$$\omega_{GD} = -i \left. \frac{\partial_\tau C}{C(\tau)} \right|_{\tau=0}, \tag{7}$$

where $C(\tau)$ is the temporal covariance function of the ensemble averaged electromagnetic field backscattered in the direction of the radar.

Assuming Gaussian statistics for the sea surface, introducing $\rho(\boldsymbol{\xi}, \tau) = \langle \eta(\boldsymbol{x} + \boldsymbol{\xi}, t + \tau) \eta(\boldsymbol{x}, t) \rangle$ the space-time covariance function of the sea surface elevation, and $\mathbf{Q_H}$ and Q_z the horizontal and vertical components of the Ewald vector, one obtains
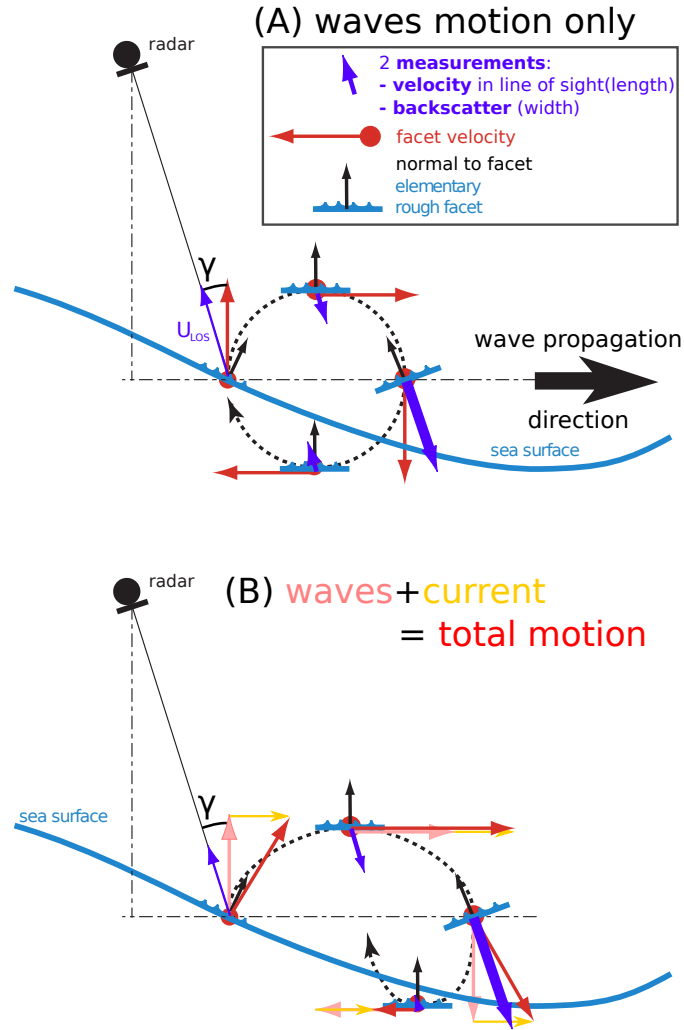
Figure 4. Schematic of (A) wave and (B) wave and current contributions to Doppler velocities at the scale of elementary facets. These small-scale processes are averaged over the radar field of view, and a mean velocity signal emerges due to the correlation of surface brightness and velocities in the wave field.

$C(\tau)$ and $\partial_\tau C$ as

$$C(\tau) = \int e^{i\mathbf{Q_H}\cdot\boldsymbol{\xi}} \left[e^{Q_z^2(\rho(\boldsymbol{\xi},\tau)-\rho(\mathbf{0},0))} - e^{-Q_z^2\rho(\mathbf{0},0)} \right] d\boldsymbol{\xi} \tag{8}$$

$$\partial_\tau C(\tau) = Q_z^2 \int \partial_\tau \rho(\boldsymbol{\xi},\tau) e^{i\mathbf{Q_H}\cdot\boldsymbol{\xi}} e^{Q_z^2(\rho(\boldsymbol{\xi},\tau)-\rho(\mathbf{0},0))} d\boldsymbol{\xi}. \tag{9}$$

The clear upwind-downwind asymmetry of σ^0 observed in the Drift4SKIM radar observations (see figure 10) shows that the Gaussian assumption, which is unable to describe such skewness-related effects, is clearly questionable. It is however the only

practical option, as going further would require prescriptions for the higher-order statistics of the sea surface which are at present not available.

The occurrence of ρ as the argument of an exponential in these integrals renders further analytical progress difficult (see however Nouguier et al., 2011). Approximate expressions can however be obtained by performing a Taylor-expansion of ρ in the neighborhood of the origin. This results in a Gaussian approximation of the integrand. The integrals can be readily evaluated, yielding:

$$\omega_{GD} \simeq -\boldsymbol{Q_H}^T \times [\nabla_{\boldsymbol{\xi\xi}}\rho]^{-1} \times \partial_\tau \boldsymbol{\nabla_\xi}\rho. \tag{10}$$

The derivatives of ρ are taken at $\boldsymbol{\xi} = \mathbf{0}, \tau = 0$, and can be expressed as moments of the directional sea state spectrum $S_d(\mathbf{k})$ as:

$$\partial_\tau \boldsymbol{\nabla_\xi}\rho = \mathbf{msv}, \ \nabla_{\boldsymbol{\xi\xi}}\rho = -\mathbf{Mss}, \tag{11}$$

where, in the notations of (Nouguier et al., 2018), $\mathbf{msv}$ stands for the "mean slope velocity" and $\mathbf{Mss}$ for the mean square slope matrix,

$$\mathbf{msv} = \left| \begin{array}{c} \mathrm{mss}_{xt} \\ \mathrm{mss}_{yt} \end{array} \right. , \ \mathbf{Mss} = \left[\begin{array}{cc} \mathrm{mss}_{xx} & \mathrm{mss}_{xy} \\ \mathrm{mss}_{yx} & \mathrm{mss}_{yy} \end{array} \right], \tag{12}$$

with

$$\mathrm{mss}_{x^\alpha y^\beta t^\gamma} = 2 \int_{\mathbb{R}^2} k_x^\alpha k_y^\beta \omega^\gamma S_d(\mathbf{k}) d\mathbf{k}. \tag{13}$$

The surface current enters through its effect on the dispersion relation of surface waves $\omega(\mathbf{k})$. In the presence of a vertically homogeneous current $\mathbf{U}$ (a detailed discussion of the effect of shear can be found in Kirby and Chen, 1989),

$$\omega(\mathbf{k}) = \mathbf{k} \cdot \mathbf{U} + \omega_0(|\mathbf{k}|), \tag{14}$$

where

$$\omega_0(|\mathbf{k}|) = \sqrt{g|\mathbf{k}|(1 + |\mathbf{k}|^2/\kappa_M^2)}, \tag{15}$$

is the dispersion relation of gravity-capillary waves in deep water, with $\mathbf{k}$ the wavevector and $k_M = 363.2 \ \mathrm{rad.m}^{-1}$ the wave number corresponding to the gravity-capillary regime transition. Introducing this expression in equation (10), and defining $\mathbf{msv_0}$ as the spectral moment obtained using the dispersion relation (15) in equation (13), one obtains the approximate DFS as

$$\omega_{GD} = \mathbf{Q_H}^T \cdot \left[\mathbf{Mss}^{-1} \times \mathbf{msv_0} + \mathbf{U} \right], \tag{16}$$

and the corresponding V_{GD} as

$$V_{GD} = -\sin(\theta) \, \mathbf{e}_\varphi \cdot \left[\mathbf{Mss}^{-1} \times \mathbf{msv_0} + \mathbf{U} \right]. \tag{17}$$

While clearly over-simplified (it is for instance independent of the electromagnetic wavelength, which is known to have a significant influence on σ^0), this expression has a definite pedagogical interest, as it allows one to distinguish a number of interesting features:

- The raw velocity projection V_{GD} accessible to Doppler radar instruments is composed of a "genuine" current component V_{CD}, equal to the projection of the TSCV along the radar line of sight, plus a "Wave Doppler" component V_{WD} induced by the natural motion of the sea surface.

- This V_{WD} component involves sea surface statistics of two different natures: the mean slope velocity vector $\mathbf{msv_0}$ and the mean squared slopes matrix $\mathbf{Mss}$. To this order of approximation it can be seen as the projection along the radar line of sight of the constant vector $\mathbf{Mss}^{-1} \times \mathbf{msv_0}$. In the rest of this article, M_{WD} denotes the norm of this vector.

- As noted in (Nouguier et al., 2018), $\mathbf{msv_0}$ is equal to one half the surface Stokes drift velocity of deep water waves $\mathbf{U_S^\infty}$. As noted in (Nouguier et al., 2016), the effective mean squared slopes matrix $\mathbf{Mss}$ components ($\mathrm{mss_{shape}}$), accounting for the electro-magnetic filtering effect and part of the non-gaussianity of the sea surface statistics can be obtained from the derivatives of σ^0 as a function of incidence angle for different azimuths.

- In simple cases such as those represented by parametric spectral forms such as the (Elfouhaily et al., 1997) spectrum used in this work, $\mathbf{msv_0}$ and the eigenvectors of $\mathbf{Mss}$ are aligned with the downwind direction, and the $V_{WD} = G_D \mathbf{Q_H} \cdot \mathbf{U_S^\infty}$ relation proposed in (Chapron et al., 2005) is recovered, with $G_D = \frac{1}{mss_{shape}}$.

- Both these statistics are however known to be influenced by waves at all scales. The asymptotic behaviours of the weighting factors as functions of the surface wave wavenumber in the gravity-waves range are $k^{3/2}$ and k^2 for the $\mathbf{msv_0}$ and $\mathbf{Mss}$ terms, respectively, while the parametric spectrum of (Elfouhaily et al., 1997), used in this work, decays as k^{-3}, leading to a logarithmic divergence for the $\mathbf{Mss}$ components, and a slow convergence of the $\mathbf{msv_0}$ components at high wavenumbers.

- The $\mathbf{Mss}$ components are sensitive to the detailed shape of the spectrum up until the short capillary-waves roll-off or to the electromagnetic cut-off, whichever is reached first.

- Estimating these terms requires knowledge on all the components of the sea state: the long gravity wave range can be measured (either in-situ, as during the Drift4SKIM campaign, or using the radar measurements themselves as intended in the SKIM context), but the high-wavenumber range can not be neglected, and its effect must be accounted for, for instance through the use of a parametric spectral form.

- The $\mathbf{msv_0}$ vector appears as a multiplicative factor, to which the inverse of the $\mathbf{Mss}$ matrix is applied. These terms thus have opposing influences on the final result: modifications of the sea spectrum which tend to increase the weight of small-scale components increase the mean slope velocity, but also, and rather more, the mean squared slope by which it is divided. A certain degree of stability of the end result is thus likely.

- On a similarly reassuring note, whereas the low-wavenumber part of the spectrum is affected by swell systems of remote origin, which have arbitrary orientations, the short waves represented by the parametric tail of the spectrum are known to be aligned with the wind direction, and to depend on local variables only (wind strength and direction, fetch).
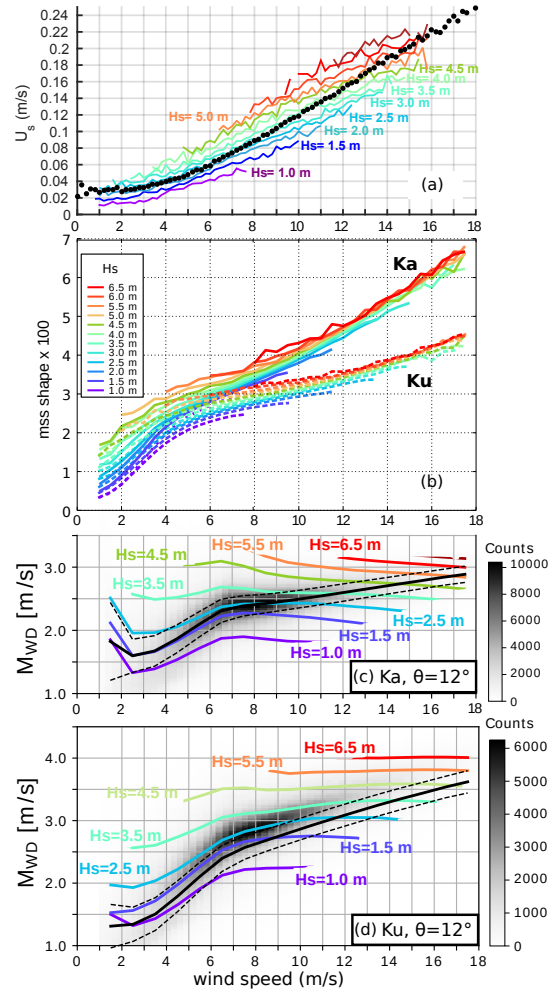
Figure 5. Computed variability of the Stokes drift velocity, the diffraction-effective mean square slope $\mathrm{mss_{shape}}$ and the Wave Doppler velocity magnitude M_{WD}. (a) 2010-2017 statistics of Stokes drift magnitude at Ocean Station Papa, computed using the buoy wind speed data and wave data from the nearby WMO buoy 46246, maintained by the University of Washington (Thomson et al., 2013). (b) $\mathrm{mss_{shape}}$ estimated from GPM satellite back-scatter using modeled co-located wind speed and wave height, reproduced from Nouguier et al. (2018). (c) and (d): Statistics of the Ka- and Ku-band M_{WD}, computed using the theoretical model of Nouguier et al. (2011) for ocean wave spectra modeled over the global ocean using the WAVEWATCH III model (Stopa et al., 2016), and plotted as a function of the wind speed. The colored curves show the median value for different classes of wave height for a given wind speed, each curve is separated by 0.5 m in (a) and (b) or 1 m in (c) and (d). In (c) and (d), the grey shading represents the histogram of the computed M_{WD} values in the global simulation.

Figure 5 gives orders of magnitude for the natural range of variability of the different factors thus isolated. Figure 5a shows the variability of the Stokes drift velocity estimated (following Kenyon, 1969; Ardhuin et al., 2009) using wind and directional wave measurements collected from 2010 to 2017 at Ocean Station Papa. Even though U_S is highly correlated with the wind speed, with a Pearson's linear correlation coefficient of 0.85, a strong dependence on the long-wavelength part of the spectrum, of which Hs is a proxy, definitely has to be accounted for.

Figure 5b, taken from (Nouguier et al., 2016), instead shows the dependence on wind speed and Hs of Ku- and Ka-bands effective mean squared slopes $\mathrm{mss_{shape}}$ retrieved from the GPM satellite measurements. The variability is even more strongly dominated by the dependence on wind speed, the variability due to the long wavelength part of the spectrum being much smaller. These measurements show very clearly the filtering effect of the electromagnetic wavelength, and are a clear warning that equation (17), suggestive though it is, should be considered with caution.

Finally, figures 5c and 5d show the magnitude of the horizontal U_{WD} component as a function of wind speed and Hs, estimated by numerically evaluating the integrals of equations (8) and (9) for $C(\tau)$ and $\partial_\tau C$ using the numerical tools of (Nouguier et al., 2011), on the basis of long-wavelength spectra extracted from global runs of the WAVEWATCH III model (Stopa et al., 2016), completed in the high-wavenumber range by (Elfouhaily et al., 1997) spectral tails. The shading in the background represents the histogram of the different (wind speed, $\mathrm{M_{WD}}$) pairs. As could be hoped for, the opposing influences of the wind speed on $\mathbf{msv_0}$ and $\mathbf{Mss}$ tend to counteract each others, greatly reducing the range of variability of M_{WD} with wind. This effect appears stronger in Ka- rather than Ku-band, possibly due to the saturation of the Ku-band $\mathrm{mss_{shape}}$ at high winds. These figures show a strong remaining impact of the long-wavelength waves, which clearly must be accounted for. As wind speed and significant height are highly correlated variables, the frequently encountered situations however fall in a quite narrow interval $M_{WD} \simeq C_0$, with $C_0 \simeq 2.6\,\mathrm{m.s^{-1}}$ and $C_0 \simeq 2.2\,\mathrm{m.s^{-1}}$ in Ku- and Ka-band, respectively. In other words, most of the variability of U_{WD} is controlled by the directionality effect and the magnitude M_{WD} is a weakly varying function of the wind, of the wave age, and the presence of swell (see also Yurovsky et al., 2019; LOPS, 2019).

A final remark is that, though these general patterns can probably be assumed robust, the precise numerical values depend on the parametric spectral shapes which have been used to fill the high-wavenumber range of the spectra. Changing for instance the high-wavenumber azimuthal spreading functions, which are for the moment not very well constrained observationally, has different impacts on the $\mathbf{msv_0}$ and $\mathbf{Mss}$ terms, and can thus be expected to marginally change the numbers.

2.3 Error Budget

Considering the errors on the different terms as independent, developing equation (1) allows one to derive the error variance of Doppler radar measurements of the TSCV as:

$$\mathrm{Var}\left(\delta U_{\mathrm{CD}}\right) = \left(\frac{U_{\mathrm{CD}}}{\tan\theta}\right)^2 \mathrm{Var}(\delta\theta) + \frac{\mathrm{Var}(\delta V_{\mathrm{LOS}})}{\sin^2\theta} + \frac{\mathrm{Var}(\delta V_{\mathrm{NG}})}{\sin^2\theta} + \mathrm{Var}\left(\delta U_{\mathrm{WD}}\right) \tag{18}$$

As a first step, four contributions to the uncertainty on U_{CD} can thus be isolated, with different origins:

- A first part corresponds merely to the error caused by the imperfect knowledge of the projection angle between the TSCV and the line of sight. Its order of magnitude is controlled by the TSCV, and it is thus negligible with respect to similar terms that involve the platform velocity.

- The second term corresponds to the random error in the DFS measurements, and subsumes the dependence on Signal-to-Noise Ratio, antenna beamwidth, orientation of the boresight with respect to the platform velocity vector and algorithmic choices. A very thorough analysis of this term can be found in (Rodriguez, 2018). The standard deviation on the raw DV signal carries over to the end result, multiplied by a $1/\sin\theta$ factor, of the order of 5 for $\theta = 12°$.

- The third term corresponds to the error caused by mismatches between the actual platform motion contribution to V_{LOS} and the estimate computed from the ancillary sensors. The order of magnitude of this term is set by the (very large) platform velocity. It is by far the largest.

- The fourth and final term corresponds to the uncertainty on the Wave Doppler removal stage. Errors in the U_{WD} model carry directly over to the U_{CD} estimates.

The third term dominates the overall error budget, and must be further analyzed. It is convenient for that purpose to start from equation (A23), which gives the expression of the beam direction vector, and use the platform velocity components in the local (North/East/Down) frame at the observation point. Neglecting terms involving the vertical velocity of the platform, and introducing the difference between the boresight and flight track azimuths $\psi = \varphi_b - \varphi_t$, one obtains the consolidated error budget as

$$
\begin{aligned}
\mathrm{Var}\left(\delta U_{CD}\right) = & \frac{\mathrm{Var}(\delta V_{LOS})}{\sin^2\theta} + \mathrm{Var}\left(\delta U_{WD}\right) + \frac{\mathrm{Var}(\delta V_D)}{\tan^2(\theta)} \\
& + \mathrm{Var}(\delta V_N)\cos^2(\phi_b) + \mathrm{Var}(\delta V_E)\sin^2(\phi_b) \\
& + V_P^2 \left[\frac{\cos^2(\psi)}{\tan^2(\theta)}\mathrm{Var}(\delta\theta) + \sin^2(\psi)\mathrm{Var}(\delta\varphi) \right].
\end{aligned}
\tag{19}
$$

This equation summarizes the dependence of the overall U_{CD} error on the errors introduced by the Doppler measurements, the U_{WD} model, the individual platform velocity components, and the incidence angle and azimuth mispointing errors.

As an illustration, table (2) summarizes the requirements that have to be met to keep the standard deviation of each of the seven terms below 0.15 m.s^{-1}, ensuring a 0.4 m.s^{-1} standard deviation for U_{CD}. The requirement on θ is translated to the corresponding altitude tracking accuracy requirement for the KuROS and SKIM configurations. The requirements on linear velocity components are stringent, but can be reached using current-day technology. The requirement on altitude accuracy is easily within the specifications of the SKIM nadir altimeter payload, but definitely out of reach of KuROS. The KuROS data could however be analysed in the cross-track looking configurations, where this requirement does not apply. The requirement on azimuthal pointing accuracy is by far the most stringent. In the airborne case, it is met for the antenna boresight by the plane IMU, allowing a straightforward analysis of the KaRADOC data. In the KuROS case, however, it is exceeded by a factor of ten by the mispointing induced by the azimuthal gradients of sea surface, which required the developement of a specific

Table 2. Standard deviations of the different error terms in equation (19) necessary to achieve a 0.40m.s^{-1} standard deviation for U_{CD}.

	KuROS 12°	KaRADOC 12°	SKIM 12°	SKIM 6°
δV_{LOS} (m/s)	$3.1\ 10^{-2}$	$3.1\ 10^{-2}$	$3.1\ 10^{-2}$	$1.6\ 10^{-2}$
δU_{WD} (m/s)	$15\ 10^{-2}$	$15\ 10^{-2}$	$15\ 10^{-2}$	$15\ 10^{-2}$
$\delta V_{\mathrm{N,E}}$ (m/s)	$15\ 10^{-2}$	$15\ 10^{-2}$	$15\ 10^{-2}$	$15\ 10^{-3}$
δV_{D} (m/s)	$3.2\ 10^{-2}$	$3.2\ 10^{-2}$	$3.2\ 10^{-2}$	$1.6\ 10^{-2}$
$\delta\theta$, up/down track (rad)	$0.26\ 10^{-3}$	—	$4.5\ 10^{-6}$	$2.3\ 10^{-6}$
δh, up/down track (m)	$17\ 10^{-2}$	—	$80\ 10^{-2}$	$20\ 10^{-2}$
$\delta\phi$, cross track (rad)	$1.2\ 10^{-3}$	$1.2\ 10^{-3}$	$21\ 10^{-6}$	$21\ 10^{-6}$

data correction procedure. Finally, in the spaceborne case, it seems only achievable using a combination of high-end inertial measurements and data-driven analysis techniques.

3 Campaign overview

This section provides a general overview of the campaign. The location, timing and overall organization are described in section
5   3.1, the environmental conditions encountered during the campaign are described in section 3.2, and the two main instruments, the KuROS and KaRADOC airborne radars, are described in sections 3.3 and 3.4, respectively.

3.1 Campaign organization

The Drift4SKIM experiment differs from previous airborne Doppler radar campaigns (Martin et al., 2016; Rodríguez et al., 2018) in two important respects: in order to observe the effect of wave development on the geophysical Doppler velocity
10   U_{GD}, it was performed in a midlatitude, eastern basin oceanic environment, open to offshore swells. Also, given the campaign objectives of demonstrating the sensitivity of airborne radar Doppler measurements to the geophysical contributions of currents and waves, it comprised an extensive in-situ component designed to have commonly accepted reference measurements for these parameters.

Field work was performed in two areas (denoted by square boxes in Figure 6) named the "offshore" area, centered on the
15   "Trèfle" buoy (see below), and the "Keller race" area, to the north of the island of Ushant. Both locations are in the range of coverage of a two-sites WERA (Gurgel et al., 1999) High-Frequency radar system, operated by Service Hydrographique et Oceanographique de la Marine (Shom) and already used for several studies, in particular related to wave-current interactions (Ardhuin et al., 2009, 2012; Guimaraes et al., 2018).

The "Keller race" is an area with very strong horizontal gradients of the current. Although it is easy to show a strong effect of
20   the current on the measured DFS, the spatial variability of the sea state is difficult to measure in situ, introducing uncertainties when combining $U_{\mathrm{CD}} + U_{\mathrm{WD}}$ in a forward model or using U_{WD} estimates when retrieving U_{CD} from the measured U_{GD}. The

"offshore" area, on the other hand, was chosen for its spatial uniformity, being located far enough from the islands and with a near-uniform depth of 110 m. Only airborne data acquired over the offshore area are presented in this paper.

The week around spring tides of November 2018 was selected, in order to allow for a wide range of current speeds (Fig. 7a).
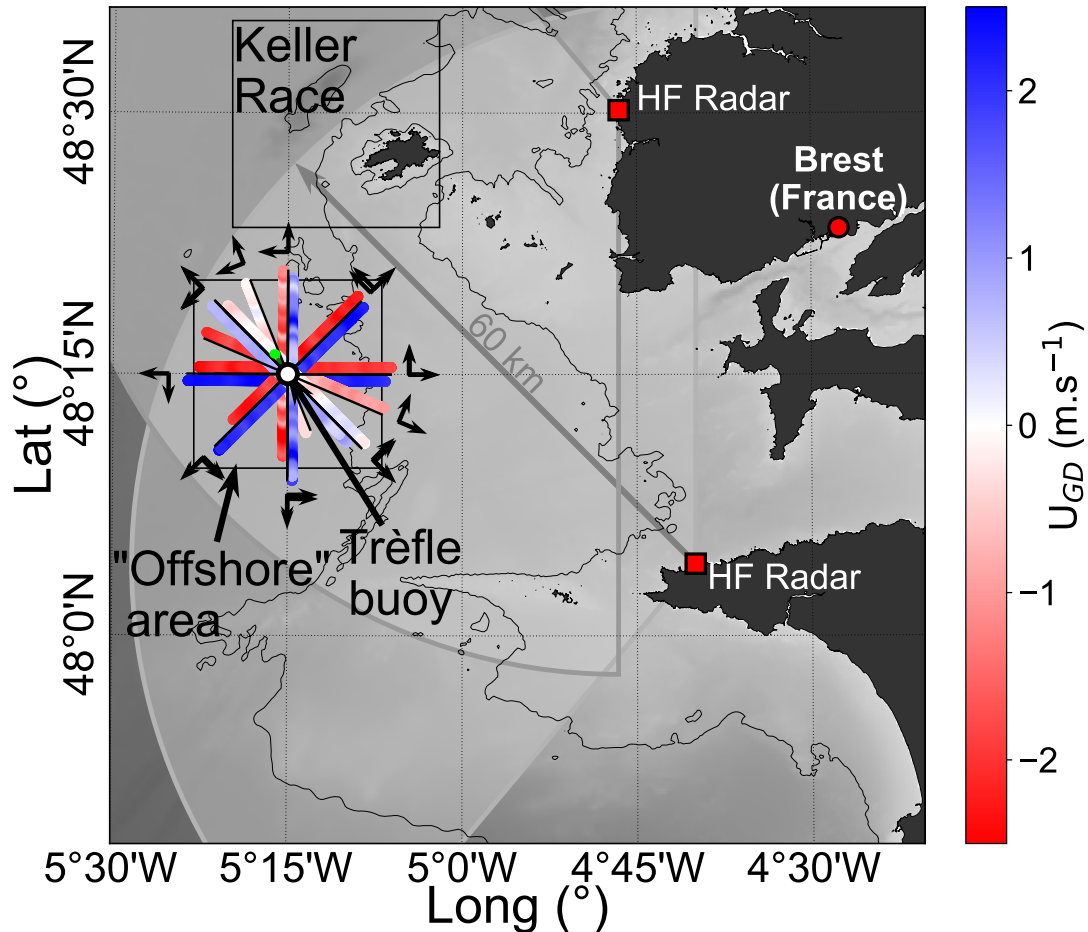
Figure 6. Location of the measurement campaign and in situ assets, including a map of the KaRADOC measurements of the Geophysical Doppler velocity U_{GD} acquired on November 22nd, 2018.

The KuROS and KaRADOC radars were installed on an ATR-42 plane operated by the French institutional scientific flight facility, SAFIRE, which is equipped with an AIRINS[TM] GNSS-FOG INS providing position, pitch, roll, heading information with stated tolerances of a few centimeters, 0.005°, 0.005° and 0.01°, respectively.

Ground truth measurements comprised two permanent operational systems: the HF radar system mentioned previously, with expected depth of measurement around 1 m (Stewart and Joy, 1974), and the "Pierres Noires" (WMO #62069) wave-measuring buoy. Dedicated instrumentation was also deployed for the campaign:

– The "Trèfle" buoy was moored at 5°15' W, 48°15' N, at the center of the "offshore" area. This buoy monitored the surface current (Sutherland et al., 2016) and provided directional wave spectra (Fig. 8).

– Several types of drifting buoys including CARTHE drifters (Novelli et al., 2017), drogued around 40 cm, SVP drifters (Niiler and Paduan, 1995), drogued at 15 m, and "Spotter" wave-measuring buoys (Raghukumar et al., 2019) were deployed in the measurement areas.

– The R/V Thalia worked in the offshore area, providing continuous underway measurements of meteorological parameters using a Météo-France "BATOS" operational system comprising a Vaisala WXT-series sonic anemometer located approximately 10 m above sea surface. The ship also carried a SBE21 thermosalinograph.

In the summer, the so-called "Ushant tidal front" has a strong influence on the surface currents, hydrographic (Le Boyer et al., 2009) and atmospheric (Redelsperger et al., 2019) conditions in the offshore area. This seasonal feature typically disappears in October, and CTD casts were performed from R/V Thalia to confirm that it had indeed vanished when the campaign took place. The water column was found to be very well mixed, with surface-to-bottom potential density anomalies being smaller than $0.002 \ \mathrm{kg.m^{-3}}$. The spatial homogeneity was also checked using the ship thermosalinograph and an infrared camera mounted on a Piper PA-23 plane which surveyed the "offshore" area in a "lawn mowing" pattern, flying under the clouds at an altitude of 500 m to 1000 m. While small-scale surface features were observed on calm days, it is clear that no density-associated mesoscale structures were present.

The airborne radar measurements geometry over the "offshore" area consisted of relatively long (12 km) and straight tracks with different aircraft headings, forming a star pattern, as for the 2018/11/22 flight shown in figure 6. Tracks were flown every 12, 22.5 or 45° in azimuth, depending on flight duration constraints. The KaRADOC antenna was fixed relative to the aircraft and looking to port, while the KuROS antenna could either be fixed in the uptrack or port cross-track directions, or rotate in the clockwise sense relative to the flight track. The KuROS Doppler data presented in this paper were acquired in the port-looking configuration.

3.2 Geophysical conditions

A wide range of geophysical conditions were encountered during the one-week-long campaign. Four flights were performed over the "offshore" area, on 11/21 from 13:50 to 15:50, on 11/22 from 12:15 to 15:00, on 11/24 from 11:20 to 13:20, and finally on 11/26 from 09:40 to 11:00. In this paper, we focus on data acquired on 11/22 and 11/24 as the geophysical conditions were interesting and complementary (see below) and data were acquired with the largest azimuth diversity on these two days.

The November 22nd flight took place at the end of a steady southeasterly wind episode (13 m/s from 140°). The November 24th flight in contrast took place during a steady weak south-westerly wind period (5 m/s from 225°) (Fig. 7b).

The wave height during the campaign was dominated by the presence of two swell systems from North Atlantic remote storms. The swell height decreased from 2.5 m on November 21st to 0.9 m on the 24th, with a peak frequency increasing from 0.07 Hz to 0.1 Hz, and a mean direction gradually veering from north-west to west. This swell has a small contribution to the Stokes drift, of the order of 10% of the windsea contribution on November 22nd.
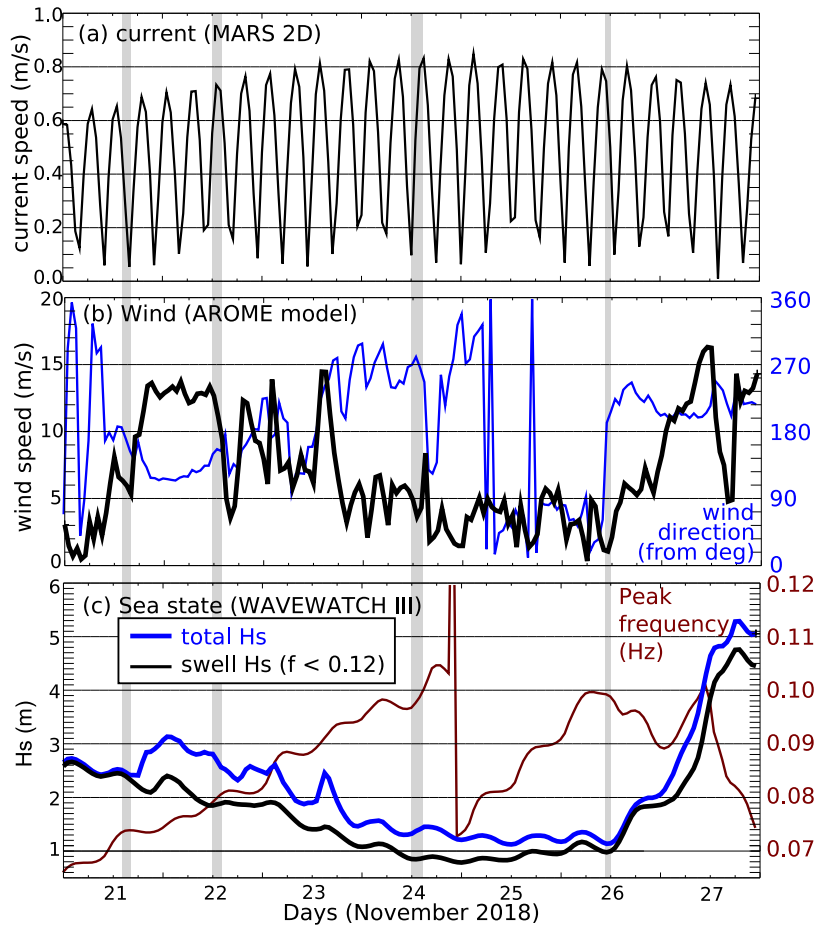
Figure 7. Time series at the location of the Trèfle buoy (5°15' W, 48°15' N) in the offshore zone of (a) ocean surface current speed from the MARS2D numerical model run at LOPS (Lazure and Dumas, 2008); (b) wind speed (black) and direction (blue) from the AROME regional operational model run by MeteoFrance, and (c) total (blue) and swell (black) significant wave height and wave peak frequency (red) from the WAVEWATCH III numerical wave model run at LOPS (Roland and Ardhuin, 2014). The four time periods shaded in grey correspond to the times of fixed-antenna KuROS measurements. The corresponding observed environmental parameters are detailed in table 3.

The main environmental conditions at the time of these star-pattern flights are summarized in Table 3.

3.3 KuROS instrument

KuROS is a Ku-Band (13.5 GHz) pulse pair Doppler radar with a dual antennae system and azimuthal scanning possibility, which was developed in the framework of the CFOSAT pre-launch studies. Of the two antennas, the Low Incidence (LI) antenna is nominally centered on 14° incidence angle, while the Medium Incidence antenna is nominally centered on 40° incidence angle. Only the LI antenna, which was the more relevant for SKIM, was used during the campaign. This antenna uses a HH
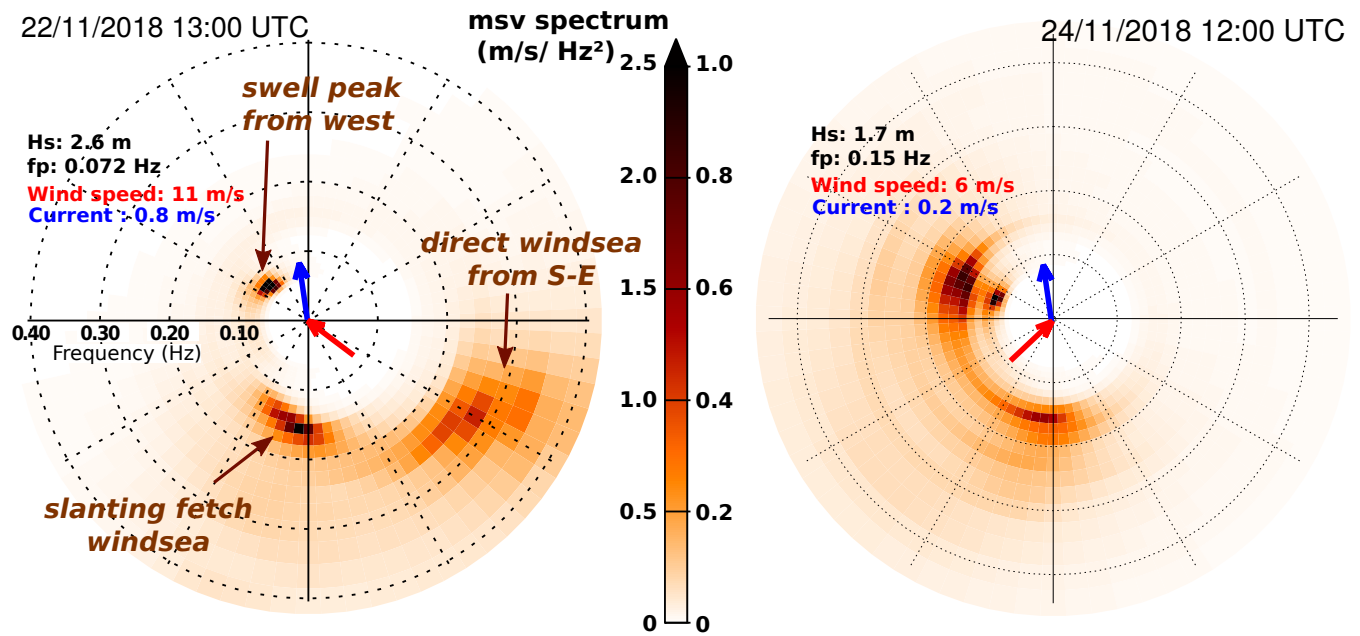
Figure 8. Directional wave spectra $E(f_r, \theta)$, as functions of the relative wave frequency f_r and incoming waves azimuth θ, estimated from the motions of the Trèfle buoy on 11/22 at 13:00 UTC and Spotter buoy number 10 on 11/24 at 12:00 UTC. The measured directional moments were transformed with the Maximum Entropy Method (Lygre and Krogstad, 1986), and Doppler shifted with $f_r = f - \mathbf{k} \cdot \mathbf{U}/(2\pi)$ for the moored Trèfle buoy. The red and blue arrows represent the AROME wind and MARS2D surface current vectors directions, respectively.

polarization. A comprehensive description of the system can be found in Caudal et al. (2014). A new antenna was used for the Drift4SKIM campaign, with characteristics given in Table 1.

The radar transmits a frequency-modulated pulse (chirp) with a 100 MHz bandwidth, achieving a 1.5 m range resolution and an effective ground-projected resolution of approximately 7 m (at 12°). The 1-way 3-dB footprint in azimuth is 580 m wide at 12° and 3000 m flight altitude. The Pulse Repetition Frequency (PRF=1/PRI) depends on the altitude, and is 23 kHz when the aircraft flies at 3000 m. The ambiguity on the Doppler velocity measurement (see section A1.4 in the appendixes) is about 126 m/s, which is much larger than expected from the measurements (below aircraft speed of 120 m/s). In order to reduce the thermal noise contribution, the range-resolved pulse-pair signal is coherently averaged in the instrument over 1 ms, corresponding to 22 pulse pairs per intrument sample. For the purpose of this article, this was further coherently averaged per blocks of 15 sample.

As discussed in Appendix A, accuracy requirements on observation geometry are much less stringent for cross-track than for up/down-track Doppler velocity observations. The Doppler velocity data discussed in this article were all collected with the KuROS antenna in the port-looking orientation. This configuration also ensures an overlap with the KaRADOC footprint.

Table 3. Velocities of current and Stokes drift measured or estimated near position 48°15' N, 5°15' W, in cm/s, and wind vector components in m/s. Please note that the Stokes drift is only integrated up to 0.5 Hz. Buoy data correspond to the Trèfle buoy for 11/22 and Spotter buoy number 10 for 11/24.

Time	CARTHE	SVP	HF-radar	buoy (U_s, V_s)	WW3 (U_s, V_s)	wind (ship)	wind (Arome)
11/21 14:00	(18,72)	(21,72)	(26,69)	(0.69, 2.23)	(0.44,2.06)	(-0.0,7.3)	(0.5,6.3)
11/21 14:30	(17,58)	(19,58)	(25,58)	(0.88, 2.02)		(-4.3,6.9)	-
11/21 15:00	(15,45)	(16,49)	(17,41)	(0.21 2.54)	(0.41,2.12)	(-4.5,5.0)	(-1.1,5.8)
11/21 15:30	(15,22)	(15,21)	(16,26)	(0.23, 1.97)		(-4.7,7.8)	-
11/22 12:00	(-2,73)	(-3,81)	(-5,58)	(-5.47,8.86)	(-7.38,11.55)	(-9.1,7.1)	(-6.8,10.7)
11/22 12:30	(-3,97)	(4,84)	(2,71)	(-5.44,9.19)	(-7.42,11.37)	(-9.4,7.2)	-
11/22 13:00	(6,102)	(4,94)	(7,84)	(-4.72,8.37)	(-7.07,11.39)	-	(-5.2,10.0)
11/22 13:30	(10,85)	(12,89)	(14,88)	(-4.75,8.02)	(-6.68,11.50)	(-4.5,9.1)	-
11/22 14:00	(9,82)	(12,87)	(23,81)	(-3.28,7.19)	(-6.35,11.66)	(-3.9,11.1)	(-4.4,8.3)
11/22 14:30	(10,78)	(11,78)	(25,72)	(-3.35,6.93)	(-5.82,11.76)	(-7.4,7.1)	-
11/24 11:30	(-10,-2)	(-11,-6)	-	(2.47,1.81)	-	(3.8,2.9)	-
11/24 12:00	(-6,19)	(-7,16)	-	(2.49,1.20)	(0.75,2.92)	(4.0,3.8)	(4.9,0.1)
11/24 12:30	(-2,40)	(-1,40)	-	(2.92,1.66)	(0.68,2.71)	(4.8,2.9)	-
11/24 13:00	(-1,60)	(1,59)	-	(3.20,1.35)	(0.68,2.71)	(4.5,2.0)	(3.5,-0.7)
11/24 13:30	(-1,77)	(2,78)	-	(2.73,1.29)	(0.70,2.60)	(3.4,2.8)	-
11/26 10:00	(-19,-83)	(-20,-87)	(-25,-62)	(0.46,-0.19)	(0.59,-0.64)	(-2.0,0.5)	(-1.0,-0.6)
11/26 10:30	(-22,-80)	(-24,-84)	(-28,-63)	(0.32,-0.23)	(0.59,-0.64)	(-1.0,1.4)	-
11/26 11:00	(-20,-74)	(-27,-74)	(-33,-66)	(0.30,-0.20)	(0.59,-0.64)	(0.6,1.4)	(0.2,1.1)

3.4 KaRADOC instrument

The Ka-band RADar for Ocean Current monitoring (KaRADOC) airborne radar sensor was developed for the Drift4SKIM campaign. KaRADOC is derived from the Still WAter Low Incidence Scattering (SWALIS) instrument, developed for the measurement of the NRCS of inland water surfaces in Ka-band. Further details on the system are given in Appendix C.

5 KaRADOC was mounted under the ATR-42 aircraft, in a port-looking configuration. The two-way 3 dB footprint from 3000 m altitude over a flat sea surface is an ellipse with diameters 45 and 60 m in the cross-track and along-track directions, respectively. The incidence angle is selected by varying the working frequency. Data were acquired at different incidence angles, from 6 to 14°, corresponding to a change of frequency from 32.5 to 38.2 GHz. This article focuses on the observations collected at $\theta = 12°$, at 33.7 GHz.

10 KaRADOC does not implement a range-resolution scheme: the transmitted pulses last several μs, and the whole FOV is illuminated simultaneously. The demodulated return signal is sampled at 15 MHz and archived. It is essentially constant

while the electromagnetic wave is actually interacting with the sea surface. The useful signal segment is selected and its average is computed in order to reduce the thermal noise contribution, yielding one complex amplitude for each pulse. Several hundred pulses are sent at 4 kHz PRF for each burst of measurements, with a burst repetition frequency of the order of 5 to 10 Hz, depending on the number of incidence angles in the scanning sequence. These parameters have been varied during the acquisitions. Though they have a strong impact on NRCS and DFS estimates quality, we have found the low-pass filtered DFS signal to be robust.

The pulse pair complex signal is averaged for each burst, in order to reduce the effect of coherent speckle. One complex pulse-pair sample is thus obtained per burst. Even at the lowest burst repeat frequency of 5 Hz, the plane moves by less than a third of the FOV along-track extension between bursts.

The impact of the acquisition parameters on the KaRADOC measurements normalization is not yet fully understood, and the NRCS measurements could not be exploited in the scope of this study. The noise-filtered DFS measurements are however not affected by these normalization changes, and are valid.

4 Measurements

4.1 KuROS NRCS / DFS imagery

The KuROS NRCS / DFS imagery reveals a host of interesting features, modulations and dependencies. An in-depth analysis of all these processes is clearly out of scope of this paper, and will be the subject of forthcoming contributions from the Drift4SKIM team. This section thus only provides a cursory description of a few segments of σ^0 and DV data collected on November 22nd, 2018, when the wind speed was approximately 11 m.s^1, which are displayed in figure 9.

A first remark is that the NRCS is smooth, with a typical modulation depth of 1 dB after removing its mean trend as a function of incidence angle (Fig. 9.A). This smoothness is in part due to the large footprint, but also shows that the radiometric quality of the data and the coherent averaging performed are sufficient to control the thermal noise. Speckle noise is however still present, with different statistics depending on the radar look direction and the variable considered (not shown). The cross-track observation geometry leads to the best speckle noise reduction for the NRCS, but to the worst-case speckle noise statistics for the DV.

The KuROS data clearly show a modulation, both in NRCS and U_{GD}, associated to the north-westerly swell observed by the Trèfle buoy with a peak frequency of 0.07 Hz, corresponding to a wavelength $L = 320$ m (Fig. 8). This is particularly visible on the north-south oriented flight tracks numbered 5 and 6 in Fig. 9.B (see also Figs. 9.F-G for a zoom on track 6). The apparent swell crests direction (dashed lines in figure 9.B) differs from the true direction due to the scanning distortion effect (Walsh et al., 1989; Sutherland et al., 2018), as the swell propagates during the measurements at a phase speed of 22 m/s, while the aircraft moves at 120 m/s.

The shorter waves measured by the Trèfle buoy (Fig. 8) occupy a wide range of directions from a narrow windsea peak from the south at 0.16 Hz ($L = 60$ m), to a broad directional distribution at 0.22 Hz ($L = 30$ m) with a mean direction of 130° and a half width (spread) of 45°, hence covering directions from 85° to 175°. These shorter components are present in the data from
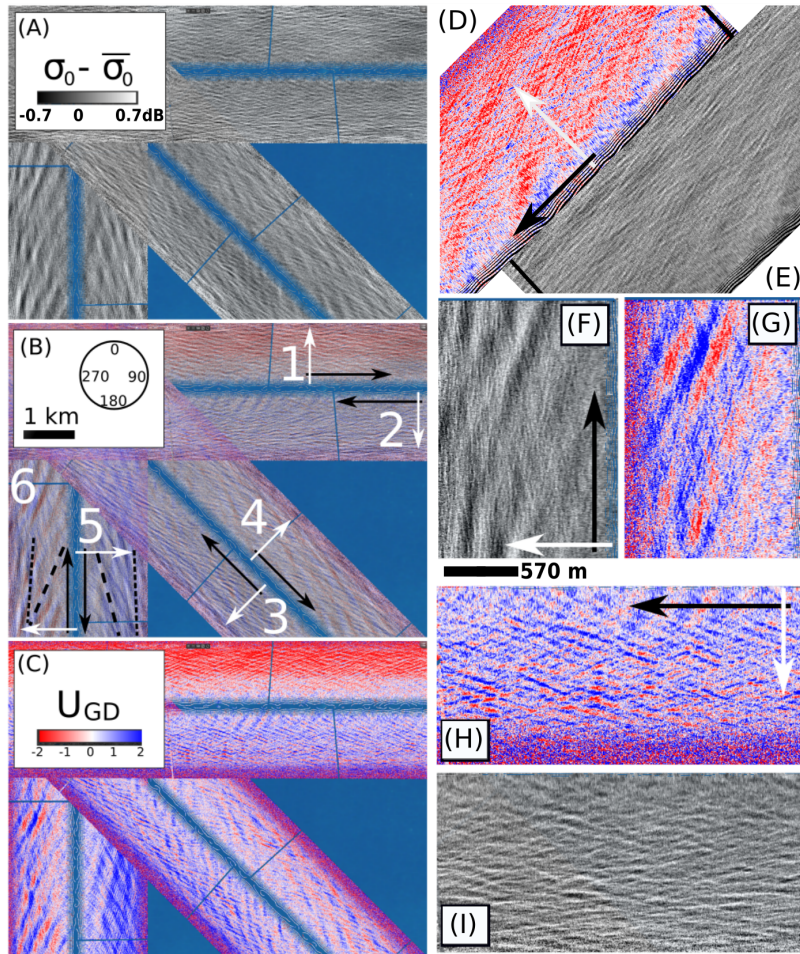
Figure 9. (A) and (C) Mosaics of KuROS backscattering intensity and Doppler velocity data acquired on November 22nd with fixed port-looking antenna. (B) overlay of the Doppler velocity and backscattering intensity. Flight tracks are numbered 1 to 6, black arrows indicate the flight direction and white arrows point in the radar look direction. The long dashed lines represent the apparent direction of swell crests. (D)-(I) are close-up views of selected tracks from (A) and (C). The tracks shown in (D) and (E) are out of the frame of (A) and (C). (F)-(I) show close-ups of flight tracks 6 and 2. The 570 m scale bar applies to (H)-(I) and correspond to the along-track 3-dB width of the radar beam at 12° incidence angle, i.e. near the middle of the swath. The mean trend of σ^0 as a function of θ has been removed from the σ^0 data.

flights tracks 5 and 6, in the form of very narrow stripes with orientations shown with the short dashed lines in 9.B (see also Figs. 9.F-G for a zoom on track 6). The "long-crested" appearance of the short waves in (D) and (E) is an artefact due to the wavefront-matching observation geometry (Jackson et al., 1985), with all other directions averaged out by the large azimuth width of the radar beam. If purely geophysical, the phase relationship between the DV and NRCS modulations is expected to give the wave propagation direction. For flight track 6 in (F) and (G), the long swell propagates towards the radar and the brighter slopes (white) correspond to eastward velocities toward the radar (blue). This will be discussed in further details

below. Finally (H) and (I) exhibit chevron patterns with crests facing both north-east and nort-west directions. Whereas the waves from the south-west are expected to be much longer than those from the south-east, this is not apparent in the KuROS data.

4.2 Ku-band NRCS

5   In this section we discuss the dependence of the Ku-band NRCS as a function of azimuth and incidence angle, for the November 22nd and November 24th cases. The fixed-antenna as well as the rotating-antenna data are presented. In order to reduce the dispersion introduced by the short-scale modulating processes discussed above, the data were averaged per $1°$ incidence angle and azimuth bins. As mentioned before, full tracks are straight and relatively long (12 km), and view a mainly homogeneous ocean region. For the fixed-antenna observations, azimuthal diversity is obtained by performing tracks in different flight

10   directions, forming a "star" pattern.

  The variations of the Ku-band σ^0 are shown for November 22nd in Fig. 10. These measurements show the expected modulation of 0.8 to 0.9 dB with azimuth, with a downwind-crosswind contrast that increases with the incidence angle. This contrast is larger for the higher winds of November 22nd. The upwind-downwind asymmetry is expected from the behavior of the surface slope probability density function (Chapron et al., 2002; Walsh et al., 2008; Munk, 2008). The exception are the σ^0 values for

15   the flight tracks with a fixed antenna around the azimuths 90 and 270 (Fig. 10.A), which have anomalous normalized values between 1 and 1.3 instead of expected values much closer to 1. We have no explanation for this anomaly, which is genuine. No such anomaly was found for the rotating antenna data collected later on the same day (Fig. 10.B).

  Discarding these azimuth ranges (shaded in grey in figure 10.C), the data could be well fitted with a functional form $a_0 + a_1 \cos(\varphi - \varphi_{\sigma,1}) + a_2 \cos[2(\varphi - \varphi_{\sigma,2})]$. As explained in section 2.1, measuring this azimuthal variation is critical for

20   the interpretation of the mean Doppler velocity due to the spurious azimuth gradient contribution. As expected, the fitted directions $\varphi_{\sigma,1}$ and $\varphi_{\sigma,2}$ are very close to the wind direction, except for the lowest incidence angles for which the contrast is less than 0.05 dB.

  On November 24th, the σ^0 azimuthal contrast was much weaker (Fig. 11), due to the much lower wind speed, and was actually not aligned with the wind direction when the measurements were performed.

4.3 Mean Doppler Velocity from KaRADOC

We now discuss quantitatively the measured Doppler velocity signal, in order to assess the agreement of our theory of the wave-induced contribution U_{WD} with the measurements. This section is focused on the KaRADOC data, which are easier to interpret than the KuROS data due to the narrower radar beam of the instrument.

  We have presented in figure 6 the low-pass filtered U_{GD} estimates retrieved from the $12°$ incidence angle KaRADOC data

30   collected on November 22nd between 12:13 and 12:59 (TU).

  This representation is misleading, as much of the observed variability is in fact due to the effect of the flight track orientation. For instance, the largest contrast can be observed between the northeastward- and southwestward-directed flight tracks, even though to a first approximation a mere change in observation direction has occurred.
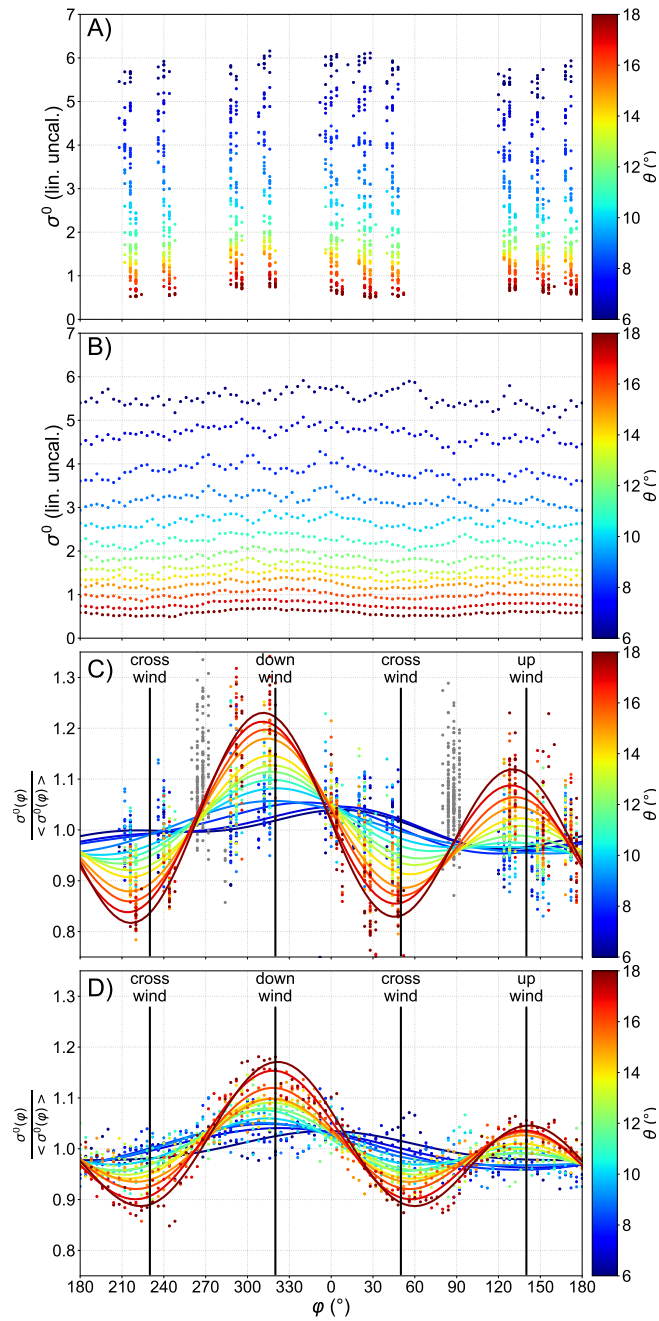
Figure 10. (A) and (B): variations as a function of azimuth φ of σ^0 for incidence angle θ 6° to 18° on November 22nd for the port-looking (12:13 → 13:38 UTC) and rotating antenna (13:41 → 13:58 UTC) flights, respectively. (C) and (D): variations of σ^0 normalized by its azimuthal average, for respectively the fixed and rotating antenna data.
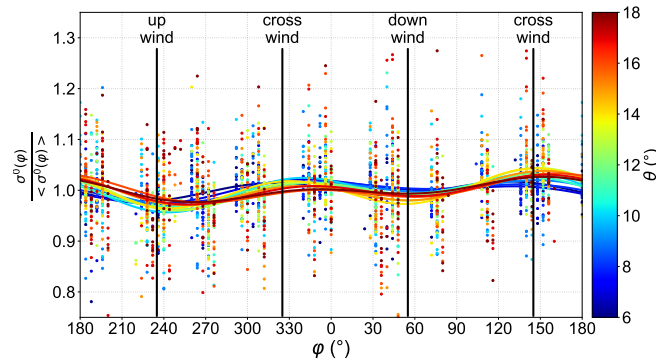
Figure 11. Same as Figure 10.C but using port-looking antenna data collected on November 24th, 11:22 → 13:03 (UTC).

Another representation of the same data is proposed in figure 12. In this figure the U_{GD} data are represented as blue lines shifted to the right of the plane ground track (in black) by an amount proportional to the instantaneous low-pass filtered U_{GD} value. This representation removes the trivial effect of observation direction changes, and allows subtler effects to be better appreciated. For instance, noise-free observations of a constant vector $U_{\mathbf{GD}}$ would appear as straight lines parallel to the flight
5 tracks, all crossing at the tip of the vector. Deviations from this behaviour, such as can be observed in figure 12, are indicative of measurement noise, of geophysical variability, or of geophysical phenomena not accounted for by our theory.

For November 22nd, 16 flight tracks are available, collected from 12:13 to 12:59 (TU), and for November 24th 17 tracks were collected from to 11:27 to 13:13 (TU).

Overall, the assumption of a constant vector is good to within 0.3 m/s. It is particularly striking that the three horizontal lines
10 in figure 12.A are almost perfectly aligned, corresponding to 2 flight tracks looking into azimuth 0° and one flight into azimuth 180°. On November 22nd, the largest dispersion is for the 315° and 135° azimuths for which a total of 4 tracks are available with very different values, that are however consistent along each track.

Now using the average values from the different tracks, we compare the measured Doppler velocity to the forward model given by equation (1), with U_{WD} estimated from the in situ wave buoy data using the tools discussed in section 2.2. The
15 method combines the buoy spectrum up to 0.35 Hz and adds a high frequency tail based on the Elfouhaily (1997) spectrum, then computes numerically the integrals of equations (8) and (9) to obtain the DFS estimate. The TSCV contribution, U_{CD}, is taken to be the drift velocity of the nearest CARTHE drifter, which is uniform to within 3 cm/s in the Offshore area (Interactive animations of all deployments and trajectories can be found at https://odl.bzh/eVRHv1TE).

Figure 13 shows the measured mean Doppler velocity and standard deviation for each track (the standard deviation is
20 representative of the order of magnitude of the short-scale modulations due to waves, not of the error bar on the mean DV). On November 22nd (Fig. 13.A), the current vector accounts for less than half of the observed magnitude of U_{GD} and it is interesting that the maximum Doppler velocity is from azimuth 147°, in between the wind direction (128°) and the up-current direction (183°). The direction of the modeled and measured U_{GD} are within 5° of each other.
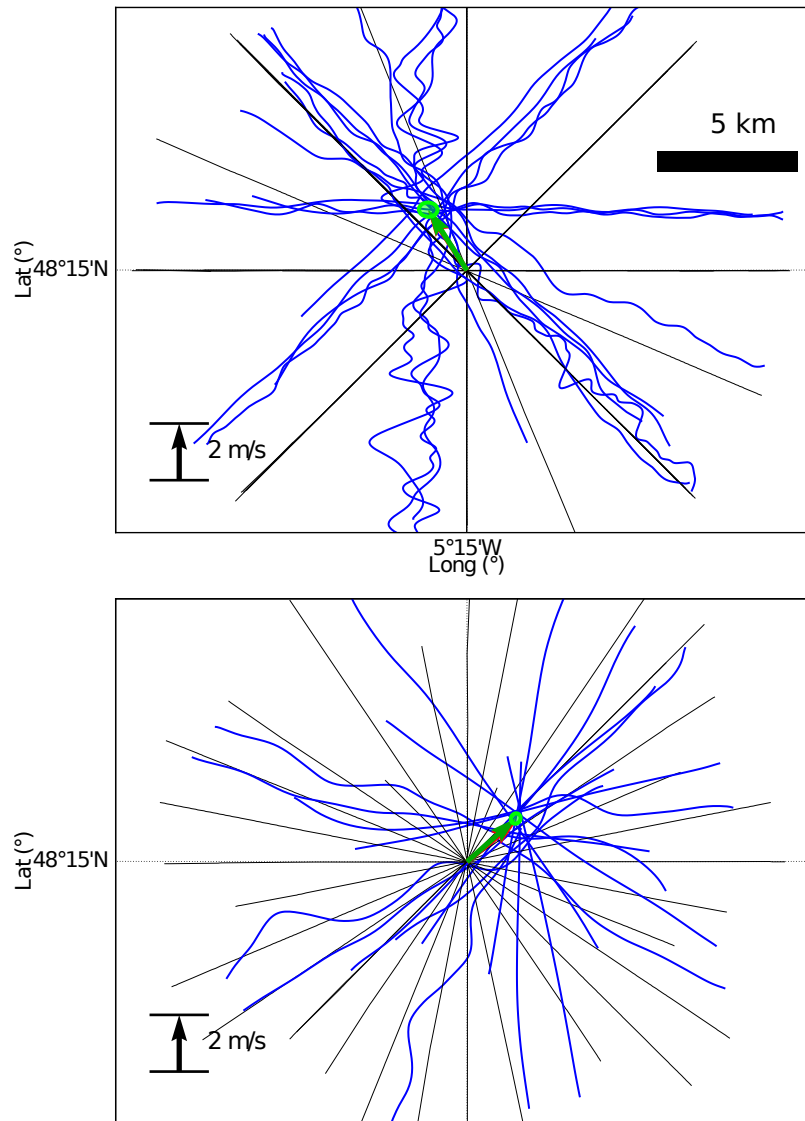
Figure 12. Plots of the Ka-band Doppler velocity signal on (top) 2018/11/22 and (bottom) 2018/11/24. The flight tracks are marked as thin black lines. For each flight track, a thick blue line shifted to the right of the flight path by an amount proportional to the instantaneous Doppler velocity represents the projection of the $\mathbf{U}_{GD}$ vector along the instrument line-of-sight. At the beginning of each track data were discarded until the plane stabilized. The green arrow represents the maximum-likelihood estimate of the $\mathbf{U}_{GD}$ vector using the whole data set. The red arrow shows the result of the least-squares sinusoidal fits shown in figures 13A and 13B. The 1-standard deviation error ellipse on the maximum-likelihood estimate is represented in green.

Compared to the relatively high wind condition on November 22nd, it is interesting to discuss the results for November 24th (Fig. 13.B), with a wind speed of 5.5 m/s instead of 11 m/s. The amplitude of the Doppler velocity is not much reduced, in spite

forward model: U_{GD} = U_{CD} + U_{WD}
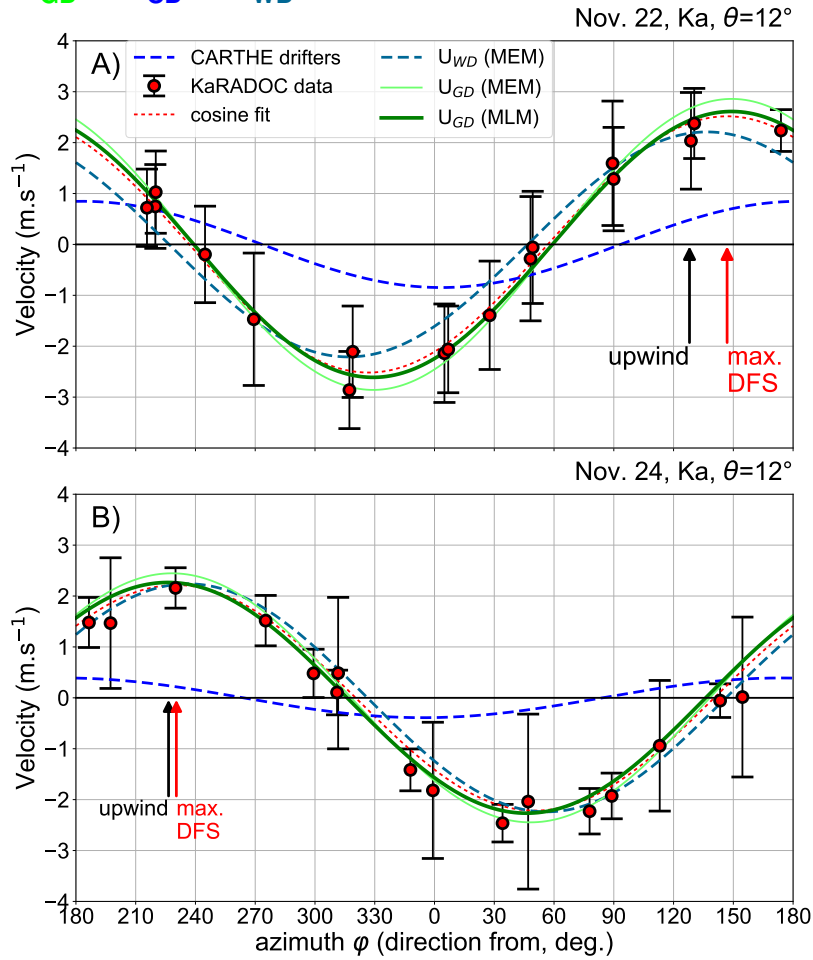
Figure 13. KaRADOC Doppler velocity (red circles) for the star-pattern flight of (A) November 22nd and (B) November 24th. Cosine function fits to the data (red lines). Modeled geophysical Doppler velocity U_{GD} using the MEM (resp. MLM) estimate of the directional wave spectrum (green, resp. darker green). The modeled U_{GD} is the sum of the CARTHE drifter velocity U_{CD} (blue) and the wave Doppler velocity estimated from the measured spectra, U_{WD} (midnight blue dashes).

of more than halved current and Stokes drift. This is consistent with the expected near-constant value C_0 of the wave Doppler velocity magnitude, and this is the main result of the present paper.

The process leading to the estimation of the constant C_0 is however dependent on a number of assumptions: the directional wave spectrum must be evaluated from the buoy data, then matched to a parametric spectral shape before the necessary numerical integrations can be performed. The (Elfouhaily et al., 1997) spectral shape we have used depends on the wind speed and direction, but also on a wave age parameter, Ω, equal to 0.84 for equilibrium seas.
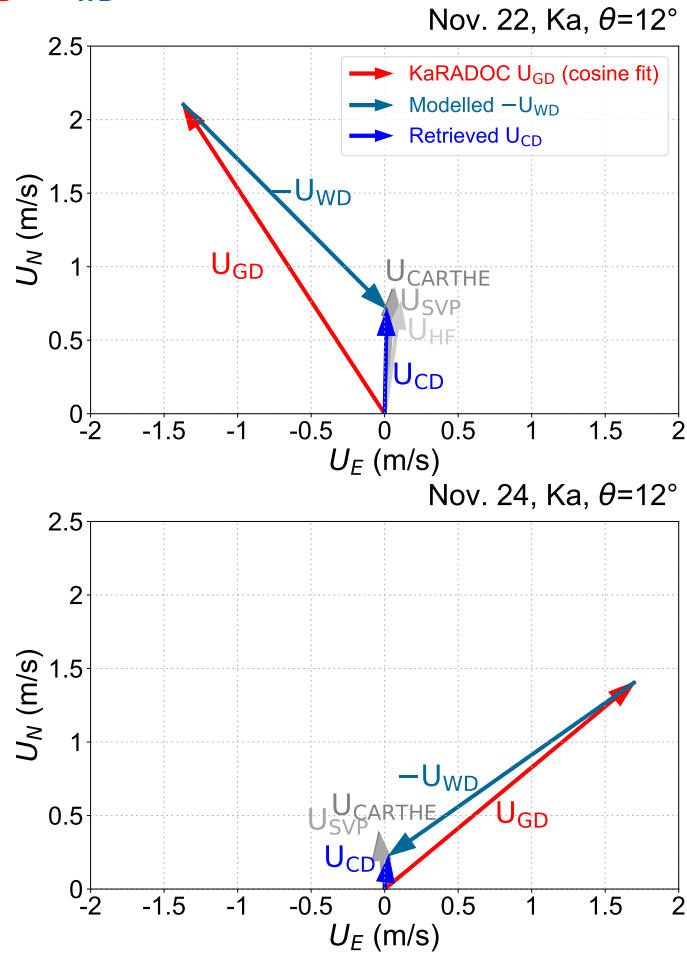
Figure 14. TSCV retrieval U_{CD} (in blue) obtained by subtracting the U_{WD} obtained from the MLM-processed Trèfle buoy data (in midnight blue) from the $U_{mathrmGD}$ vector determined from the KaRADOC measurements (in red), compared to field measurements by HF-radar, CARTHE and SVP drifters (shades of grey).

Table 4 summarizes a subset of the extensive tests we have performed to check the sensitivities of this process. It is clear from this table that changing drastically the wind speed, as occurred between the two days, affects more the magnitude of the computed U_{WD} at Ku-band than Ka-band, but not in a catastrophic way, and that the wave age parameter Ω can also be varied over its meaningful range quite freely. We have also checked that the transition frequency at which the spectral tail is matched to the observational data is not a very sensitive parameter, provided it is taken low enough for the buoy data to be of good quality where they are kept.

Extracting directional wave spectra from buoy data, however, is a quite intricate and subjective step. Several methods have been developed over the years to this end, each with pros and cons (see Benoit et al., 1997, for a review). Two of the best-

established methods are the Maximum Entropy Method (MEM) and the Maximum Likelihood Method (MLM). The MEM is a parametric method which assumes a specific form of the directional spreading function. In each frequency band, the parameters of the spreading function are chosen such that the first moments of the azimuthal Fourier spectrum match the buoy-derived ones. The MLM is a non-parametric method akin to the Capon beamformer. In terms of directional moments measured by buoys, the MEM estimates provide spectra that fit exactly the measured moments, while the MLM produces spectra that have directional spreads larger than those obtained directly from the measured moments. However, it is not clear how they compare on other properties of the spectrum that may be relevant to the mean slope velocity. Comparing results obtained with these two methods was thus a convenient way to test the sensitivity of U_{WD} to the sea state directional spread.

Table 4. Modeled wave Doppler velocity amplitude M_{WD} and direction φ_{WD} at Ku- and Ka-band, using directional wave spectra produced using the Maximum Entropy or Maximum Likelihood Methods, varying the wave age parameter Ω of the Elfouhaily (1997) high frequencies spectral tail. In all cases the transition frequency between the wave data and the high-frequency spectrum is $f_t = 0.35$ Hz. All values are estimated for $\theta = 12°$.

	Ka-band	Ku-band
11/22, 12:00 UTC	M_{WD}(m/s) / $\varphi_{\mathrm{WD}}(°)$	
MEM, $\Omega = 0.84$	2.21 / 136.7°	2.83 / 136.9°
MEM, $\Omega = 1.3$	2.21 / 136.8°	2.83 / 137.0°
MEM, $\Omega = 2.5$	2.20 / 136.8°	2.79 / 137.1°
MLM, $\Omega = 0.84$	1.97 / 135.1°	2.54 / 135.3°
MLM, $\Omega = 1.3$	1.97 / 135.2°	2.53 / 135.4°
MLM, $\Omega = 2.5$	1.96 / 135.2°	2.51 / 135.6°
11/24, 12:00 UTC	M_{WD}(m/s) / $\varphi_{\mathrm{WD}}(°)$	
MEM, $\Omega = 0.84$	2.25 / 235.7	2.50 / 235.7°
MEM, $\Omega = 1.3$	2.24 / 236.3	2.49 / 236.4°
MEM, $\Omega = 2.5$	2.17 / 237.7	2.40 / 237.9°
MLM, $\Omega = 0.84$	2.07 / 234.3	2.29 / 234.3°
MLM, $\Omega = 1.3$	2.05 / 234.8	2.28 / 234.9°
MLM, $\Omega = 2.5$	1.99 / 236.2	2.19 / 236.2°

As table 4 shows, using one technique or the other to estimate the resolved part of the waves directional spectrum does induce significant differences in the simulated U_{WD} values, showing that the azimuthal width of the spectrum, which is currently not very well constrained observationally, is a sensitive factor. The values obtained using the broader MLM spectrum are consistently smaller than those obtained using the MEM spectrum. A broader azimuthal distribution only redistributes the weight between the different **Mss** components, but reduces the contributions composing the **msv$_0$** vector.

The results obtained using both methods are shown in figure 13 as light green and dark green lines. It appears that the MLM processing of the buoy data gives the best fit to the radar U_{GD}, showing that the directional spread of the sea state should not be taken too low. The possibility that the directional distribution of the Elfouhaily (1997) spectrum could be slightly too narrow for intermediate wavelengths 2-10 m was for instance discussed in specific cases by Peureux et al. (2018). It is however not yet clear if it is specific to the very young wind seas they observed, although it could also explain some properties of L-band backscatter (Yueh et al., 2013). The MLM was used to process the Trèfle data in the rest of this study.

Conversely, figure 14 illustrates the use of the DV data for the retrieval of the surface current vector, by subtraction of $\mathbf{U}_{\mathrm{WD}}$ from the fitted $\mathbf{U}_{\mathrm{GD}}$. The norm of the difference between the in-situ measured and remotely sensed $\mathbf{U}_{\mathrm{CD}}$ vectors is less than 20 cm/s on both days, which is significant, but quite satisfying at such an early stage of the technique, especially taking into account the fact that geophysical variability due to time variations of wind and tidal current occurred over the several hours of the flight.

4.4 Mean Doppler velocity from KuROS

Due to the much broader radiation diagram of the KuROS antenna, analysing the Ku-band data requires significantly more effort, as the U_{AGD} spurious velocity contribution due to the azimuthal variation of σ^0 across the FOV discussed in section 2.1 must be compensated for. The DV measurements, corrected for the U_{NG} platform motion contribution but not for the U_{AGD} contribution, are represented in figure 15 by the red dots, while the green line represents the projection along the line-of-sight azimuth of the sum of the TSCV and the MLM-derived $\mathbf{U}_{WD}$ vectors. The difference is clearly very large, reaching $2\,\mathrm{m.s}^{-1}$ in places, on November 22nd, and smaller on November 24th as the azimuthal modulation of the radar NRCS is much weaker.

Introducing the fits to the Ku-band NRCS data discussed in section 4.2 in equation (A24) allows one to produce the corrected data represented by the magenta dots, which are in much better agreement with the green line (though a constant offset is apparent on the November 24th data, which is rejected by the cosine-fit procedure). Figure 16 summarizes then the U_{CD} retrieval operation in vector form (the magenta arrow represents only the first azimuthal harmonic component of the U_{AGD} correction). The norm of the difference between the in-situ (in grey) and remote-sensed (in blue) estimates of the TSCV is of the order of $0.5\,\mathrm{m.s}^{-1}$ on November 22nd, and of the order of $0.2\,\mathrm{m.s}^{-1}$ on November 24th. Again, these numbers, though admittedly not small, can be considered encouraging given the number of very large corrections applied to the data and the fact that the instrument had definitely not been designed for this purpose.

4.5 Observed Doppler velocity modulations

The range-resolution scheme implemented in KuROS makes it a very interesting instrument for the analysis of DFS and NRCS modulations. In particular, Caudal et al. (2014), with a different antenna (slightly narrower beam) have attempted to use the cross-spectrum of the DFS and NRCS to resolve the 180° ambiguity in the wave propagation direction. In the SKIM context, analysing the contribution of the resolved scales to the correlation between σ^0 and the DFS could permit the developement of empirical methods to estimate the unresolved part and provide estimates of U_{WD}.

forward model: KuROS U$_{GD}$ - U$_{AGD}$ = U$_{CD}$ + U$_{WD}$
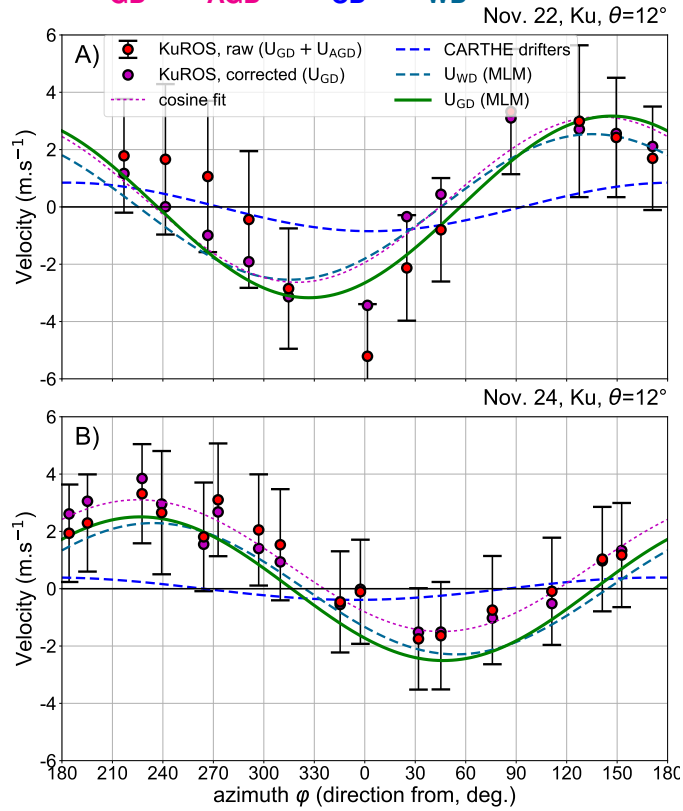
Figure 15. Ku-band Doppler measurements performed on (A) November 22nd and (B) November 24th with the KuROS radar in the port-looking antenna configuration at $\theta = 12°$ incidence angle. The graphical conventions are identical for the two plots. The red dots and error bars represent the average and ± 1 standard deviation interval of the platform-motion-corrected DV measurements along the different tracks. The magenta dots mark the mean values after correction of the U_{AGD} contribution. The magenta dotted line is the cosine fit to the corrected data. The blue and midnight blue lines represent respectively the projection along the line-of-sight azimuth of the CARTHE current measurements and the $\mathbf{U}_{WD}$ vector computed from the MLM-processed Trèfle buoy data. The green line represents the sum of these two contributions, and should agree with the magenta dotted line.

In practice, with the antenna used for the Drift4SKIM flights, another contribution to the DFS modulations is also caused by the gradients of σ^0 and the speed of the aircraft, just like the mean spurious U_{AGD} velocity. Brighter areas in the field of view tend to influence strongly the DFS signal towards positive values if they are located to the front of the aircraft, and negative values if they are located aft of the aircraft.

5 As a test of this, simulations were performed with the Radar Sensing Satellite Simulator (Nouguier, 2019), which are illustrated in Figure 17. The amplitude of the spurious modulations are enhanced by 70% when the antenna diagram is made 50% wider in azimuth. With typical variations of σ^0 up to 1 dB over scales of the order of 1 km (e.g. Fig. 9), the variation of σ^0 with azimuth φ is roughly proportional to $1/\sin\theta$ giving a U_{AGD} that does not vary much with θ, of the order of 1.5 m/s.

retrieval: U_{CD} = (U_{GD}+U_{AGD}) -U_{AGD} -U_{WD}
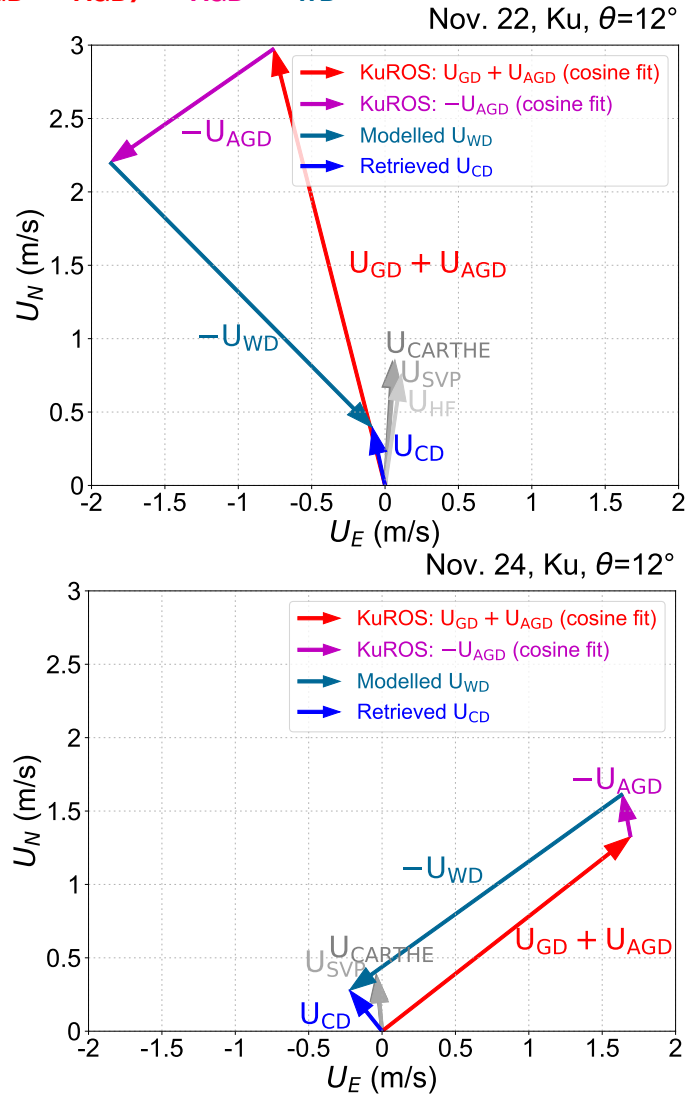
Figure 16. Comparison of KuROS-derived Doppler velocity, corrected for the U_{AGD} and U_{WD} wave contributions , with in situ (CARTHE, SVP drifters and HF radar) current measurements.

This spurious velocity is larger than the 0.5 m/s significant orbital velocity of the swell. As a result the phase relation between DFS and σ^0 can change sign as a function of azimuth, due to the combination of two imaging mechanisms with comparable magnitudes and possibly opposite signs.

This effect will be weaker for shorter (wind sea) components as soon as the wavelength and crest length becomes much shorter than the KuROS footprint L_y, as given by eq. (A36): for a given σ^0 contrast, the gradient increases linearly as the scale L is reduced, but the U_{AGD} for a given gradient is reduced exponentially in $-L_y/L$.
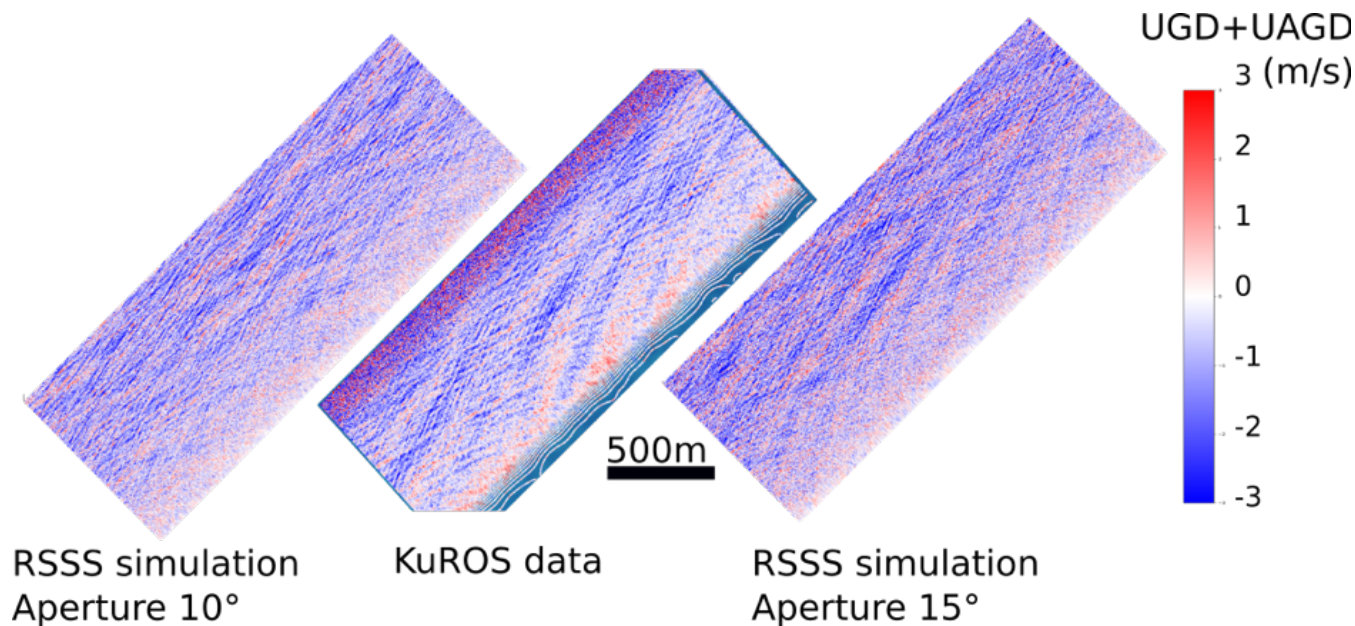
Figure 17. Qualitative validation of the R3S simulations of the radar imaging mechanism (Nouguier, 2019). Both the real data and simulation contain the geophysical modulation of velocities associated to surface velocities and slopes in the look direction (part of U_{GD}) and aircraft velocities and slopes in the flight direction (part of U_{AGD}). Note that the wave phases in the R3S simulation are random and cannot be expected to match those in the data or between the two simulations.

5   Implications for SKIM

The use of two Doppler radars, in Ka and Ku band, using the same pulse-pair technique but antennas with very different radiation diagrams, has provided important insight for the preparation of the SKIM mission.

Regarding radar measurements, the Drift4SKIM campaign clearly demonstrated the feasibility of the TSCV retrieval approach proposed for SKIM (Ardhuin et al., 2018; ESA, 2019), based on the use of the SKIM wave spectrum measurements (here replaced by in-situ buoy measurements) to estimate the wave Doppler velocity contribution U_{WD} associated with the waves intrinsic phase speed. Measuring the first directional moments (on which the buoy estimates are based) is sufficient to estimate U_{WD} and resolving wavelengths of 15 m (a frequency of 0.32 Hz) is sufficient to estimate the full spectral contribution, appending a parametric spectral shape for the unresolved shorter waves. In fact it is most important to resolve the peak of the windsea, and a resolved wavelength of 30 m is typically enough for wind speeds higher than 7 m/s. As this article has shown, however, the angular distribution of the directional spectrum is a sensitive element, both in the resolved and parameterized wavelength ranges. Work is still needed to improve the spectral parameterization and to determine whether the accuracy of the sea state restitution algorithms intended for SKIM will be sufficient to solve this issue.

This experiment has also increased confidence in the use of forward models based on the Kirchhoff approximation, such as the R3S of (Nouguier, 2019), for the study of higher-order effects on the measured DFS. A subject of particular interest

is for instance the effect of shear in the surface layer on the SKIM DFS, a key to the determination of the effective SKIM measurement depth.

The campaign also stressed the necessity of a very good knowledge of the measurement geometry, including antenna radiation diagram, and the spatial and azimuthal variation of the radar cross-section. In this respect, the main characteristics of the instruments used for the present campaign and of the planned SKIM satellite mission are recalled in table 5, together with the value of the prefactor of the $\sin(\varphi - \varphi_t)\partial_\varphi \log(\sigma^0)$ term in the expression (6) of U_{AGD} (as can be seen in figure 10, $\partial_\varphi \log(\sigma^0)$ is typically $0.1\,\mathrm{rad}^{-1}$ at $12°$ incidence angle). As the apparent mispointing due to σ^0 gradients in azimuth or space is proportional to the beam width squared, the non-geophysical velocities caused by this effect for SKIM, though non negligible, are actually much smaller than for KuROS, even at $6°$ incidence angle.

Table 5. Main differences between the KaRADOC and KuROS airborne radars used in the present article, and the SKIM system as presented by ESA (2019). The factor $\sigma_\varphi^2 V_p/2$ is the prefactor of $\sin(\varphi - \varphi_t)\partial_\varphi \log(\sigma^0)$ in the expression of U_{AGD}.

	KuROS 12°	KaRADOC 12°	SKIM 12°	SKIM 6°
Altitude (km)	3	3	832	832
platform velocity V_p (m/s)	120	120	7000	7000
Beam width ($\alpha_{-3\mathrm{dB}}$) (°)	15.0	1.85	0.65	0.58
Gaussian fit parameter σ_φ (°)	30.6	3.8	1.32	2.36
$\sigma_\varphi^2 V_p/2$ (m.s^{-1}.rad)	17	0.26	1.9	5.9

As discussed in section 2.3, due to the much reduced platform velocity, the pointing requirements for airborne systems are much easier to reach than for satellite systems for which a pointing accuracy of a few microradians cannot be achieved by attitude measurements alone (gyroscopes and star-trackers) but must use a separation of the geophysical and non-geophysical patterns in the data (ESA, 2019). This data-driven approach is also used in airborne systems for correcting phase biases in the antenna diagram (Rodríguez et al., 2018).

Finally, as discussed in section 2.3, we recall that the incidence angle is estimated from the range measurements in the cases of KuROS and SKIM, and directly from the platform attitude for the pencil-beam case of KaRADOC. In the spaceborne context, the local slope of the ocean has to be taken into account, as it can induce a mispointing of the nadir beam of up to 300 microradians (Sandwell and Smith, 2014), and induce a correction in the elevation angle at the observation point.

Other radar system constraints or optimizations for satellite systems are discussed by Rodriguez (2018) and (ESA, 2019, chapter 5), with sampling issues further analyzed by Chelton et al. (2019).

6 Conclusions and perspectives

The Drift4SKIM campaign clearly demonstrated that surface geophysical velocities can be measured by microwave Doppler radars implementing the pulse-pair method at Ka-band at $12°$ incidence angle. The Ku-band measurements, though less easy to interpret due to the large antenna beamwidth of the instrument, also supported this view. The campaign data are consistent

with a Geophysical Model Function (GMF) that expresses the geophysical DFS as the sum of the range component of the Total Surface Current Velocity, and a waves DFS that is a weakly varying function of the sea state, of the order of 2.0 m/s at Ka-band, and 2.4 m/s at Ku-band. This waves DFS integrates contributions of all wavenumbers and directions, weighted by the surface slope spectrum. It can be well estimated from the sea surface elevation directional spectrum using the Kirchhoff approximation framework.

The campaign highlighted the importance of a very good knowledge of the platform motion and orientation and of the radar line-of-sight direction vector. The Ku-band NRCS/DFS imagery, though not very successful in that respect, observed a large number of interesting modulation phenomena, which will be analyzed in more detail in forthcoming contributions.

In general, the robustness of the theoretical GMF and its possible empirical adaptation will require the acquisition of more data in a wider range of wind and wave conditions. An in-depth investigation of the angular width of the sea state directional spectrum in the short gravity waves regimes seems of particularly high interest in this respect. Also, obtaining a description of the scale-resolved statistics of sea surface slope skewness would open the path to a Kirchhoff approximation study of the upwind/downwind asymmetry of the radar NRCS and DFS, which is currently lacking.

Finally, the test of near-nadir satellite measurements is limited by the very different viewing geometry due to the difference in altitude. Airborne measurement footprints are at most 500 m or so, and thus cannot reproduce the averaging properties of the much wider footprint of a satellite instrument. Still, this medium-sized footprint is comparable to the unfocused SAR resolution that will be obtained with SKIM and provides some practical application with a similar azimuthal averaging that has a limited directional resolution for swell spectrum measurement.

Future airborne systems may ideally combine higher incidence angles such as used on DopplerScatt (Rodríguez et al., 2018) and OSCAR/Wavemill (Martin et al., 2018), with near-nadir angles that allow unambiguous wave measurements. In that case, the large azimuthal footprint of KuROS is probably not necessary, and a narrower beam like KaRADOC can be used, greatly simplifying the analysis.

Code and data availability. Data and numerical model results presented in this article are available via ftp at the following address: http://tinyurl.com/SKIMftp, and will become more easily accessible through the upcoming website of the ESA-funded IASCO project.

Appendix A: Doppler Scatterometry theory

This appendix proposes an extension of the theory of pencil-beam Doppler scatterometry exposed in (Rodriguez, 2018; Rodríguez et al., 2018) to the case of near-nadir fan-beam instruments such as SKaR and KuROS. It compiles a number of processing steps or concepts that had to be developed for the analysis of the Drift4SKIM KuROS data. In each section the differences and similarities with the spaceborne SKIM context are highlighted.

A1 Pulse pair theory

A1.1 Radar pulse-pair measurements

A radar instrument works by sending microwave pulses into the environment, and recording the echo from its field of view. Usual scatterometers consider only the intensity of the return signal. Coherent instruments, such as SARs, measure both the amplitude of the return signal and its phase with respect to the transmitted carrier, as a function of range. Over the ocean, the phase of the return signal for a single pulse is random and uniformly distributed over the unit circle. The radar returns of successive pulses transmitted at short intervals are however correlated, and the time history of the phase can be used to measure the relative motion of the radar and the scatterers. SARs make use of this property to refine the along-track resolution of backscattering cross-section measurements. SKIM and the other proposed Doppler missions aim to use it to obtain direct surface current measurements.

As explained by Rodriguez (2018, Appendix A), the complex amplitude of the return signal of a pulse transmitted at time t_i can be expressed as

$$E_i(t_i, r') = n(t_i, r') + \frac{A(r')}{r'^2} \times \int dS \, G(t_i, \mathbf{x}) \chi(r' - r(t_i, \mathbf{x})) \exp\left[-2ikr(t_i, \mathbf{x})\right] s(t_i, \mathbf{x}), \tag{A1}$$

where the integral is performed over the sea surface; $A(r')$ is a time-independent weakly-dependent function of range, unimportant for our purposes here (corresponding in particular to the effects of transmitted signal amplitude, receiver and processing gain and attenuation losses); $G(\mathbf{x})$ is the one-way antenna diagram; $\chi(r)$ is the range point-target response of the instrument; r' is the nominal pixel range in the time sampled signal; $k = 2\pi/\lambda$ is the radar wavenumber; $r(t_i, \mathbf{x})$ is the range from the radar to the observation point $\mathbf{x}$ at time t_i; $n(t_i, r')$ is the thermal noise contribution, and $s(t_i, \mathbf{x})$ is the complex reflection coefficient of the sea surface at instant t_i and location $\mathbf{x}$.

As mentioned by Rodríguez et al. (2018), the thermal noise contribution, though it plays a major role in the quality of the measurements, is conceptually simple, and can be safely considered as δ-correlated in time, and characterized by a single quantity, its average power N. The reflection coefficient $s(t_i, \mathbf{x})$, on the other hand, emerges from the interaction of the electromagnetic waves with the ocean surface, and has much richer physics. It is affected by electromagnetic phenomena, by the geometry and kinematics of the sea surface itself, and its statistics are further complicated by the so-called "speckle" phenomenon. As stated by Rodríguez et al. (2018) the correlation function of this coefficient as a function of time and space separation, averaged over speckle realizations, can be modelled as

$$\langle s(t, \mathbf{x}) s^*(t', \mathbf{x}') \rangle_S = \delta(\mathbf{x} - \mathbf{x}') \sigma^0(t, \mathbf{x}) \gamma_{TS}(|t - t'|), \tag{A2}$$

with $\sigma^0(t, \mathbf{x})$ the Normalized Radar backscattering Cross Section (NRCS) in the appropriate polarization, and $\gamma_{TS}(|\tau|)$ a function describing its time decorrelation at a fixed location, due to the life history of individual scattering patches.

The so-called "Pulse-Pair" technique of (Zrnic, 1977) relies on the properties of the product of the return signals from consecutive radar pulses. Combining expressions (A1) and (A2) to compute the speckle-averaged product of the return signals

for two radar pulses sent at t_1 and $t_2 = t_1 + \Delta t$, with Δt the pulse repetition interval (PRI), one obtains:

$$PP_{\Delta t}(t_1, r') = \langle E_2(t_2 = t_1 + \Delta t, r') E_1(t_1, r')^* \rangle_S \tag{A3}$$

as

$$PP_{\Delta t}(t_1, r') = \frac{A^2(r')}{r'^4} \times \gamma_{TS}(|\Delta t|) \times \int \chi^2(r' - r(t_1, \mathbf{x}))\, G^2(t_1, \mathbf{x})\, \sigma^0(t_1, \mathbf{x}) \times \exp\left[-2ik\left[r(t_1 + \Delta t, \mathbf{x}) - r(t_1, \mathbf{x})\right]\right] dS. \tag{A4}$$

As can be seen in this equation, the phase of the pulse-pair signal contains a weighted average of the time rate-of-change of the distance separating the radar from the scattering elements in its instantaneous footprint. This rate of change can be interpreted as a velocity.

A1.2 Measurement geometry

Figures 1A and 1B summarize the acquisition geometry in the airborne and space-borne settings. The antenna radiation diagram $G^2(t_1, \mathbf{x})$ is represented as a grey shading of the sea surface, while the range point-response function $\chi^2(t_1, r' - r(t_1, \mathbf{x}))$ is represented as a white grating. In eq. (A4), we have made the assumptions that $G(t_1, \mathbf{x}) = G(t_2, \mathbf{x})$, and $\chi(r' - r(t_1, \mathbf{x})) = \chi(r' - r(t_2, \mathbf{x}))$, neglecting the effect of the spatial translation of the beam illumination pattern and range-resolution weighting distribution on the sea surface.

This is a very good approximation for airborne pulse-pair radar observations, and a quite good one for spaceborne observations. For airborne instruments, the PRI is usually chosen such that the line-of-sight projection of the platform movement over a PRI is smaller than one-half carrier wavelength to avoid phase ambiguity. For space-borne instruments, avoiding ambiguity is not practical, due to the much larger platform velocity, but the PRI is constrained by other considerations, and the platform displacement over a PRI is much smaller than the characteristic scales of the antenna radiation diagram as well as of the range point-response.

A1.3 Pulse-pair signal approximation

Returning to expression (A4), we see that over the time interval separating the two radar pulses, the radar has moved from its original position $\mathbf{x}_R(t_1)$ to $\mathbf{x}_R(t_1) + \mathbf{V}_P \Delta t$, and the scatterers originally located at $\mathbf{x}$ have moved to $\mathbf{x} + \mathbf{v_s} \Delta t$ (specifying the reference frame is not yet necessary since only relative separations are important at this stage). The radar-to-scatterers vector has thus changed by $[\mathbf{v}_s(\mathbf{x}) - \mathbf{V}_P] \Delta t$. The distance change can be approximated by

$$r(t_1 + \Delta t, \mathbf{x}) - r(t_1, \mathbf{x}) = \Delta t \frac{\mathbf{x} - \mathbf{x}_R(t_1)}{||\mathbf{x} - \mathbf{x}_R(t_1)||} \cdot (\mathbf{v}_s - \mathbf{V}_R), \tag{A5}$$

where the neglected terms are of the order of $\Delta t^2 ||\mathbf{v}_s - \mathbf{v}_R||^2 / ||\mathbf{x} - \mathbf{x}_R(t_1)||^2$. Introducing

$$\mathbf{e}(\mathbf{x}) = \frac{\mathbf{x} - \mathbf{x}_R(t_1)}{|\mathbf{x} - \mathbf{x}_R(t_1)|} \tag{A6}$$

the unit vector pointing from the radar location at t_1 to the observation point (choosing either time instant is equivalent, as the difference is of the same order of magnitude as the neglected terms), the pulse-pair signal can be expressed as

$$PP_{\Delta t}(t_1, r') = \frac{A^2(r')}{r'^4} \times \gamma_{TS}(\Delta t) \times \int G^2(t_1, \mathbf{x})\, \chi^2(r' - r(t_1, \mathbf{x}))\, \sigma^0(t_1, \mathbf{x}) \times \exp\left[2ik\,\Delta t\, \mathbf{e}(\mathbf{x}) \cdot (\mathbf{V}_R - \mathbf{v}_s(\mathbf{x}))\right] dS. \tag{A7}$$

This equation is not very practical, as the relative motion of the scatterers with respect to the radar enters as the argument of an exponential integrand. Obtaining an equivalent representation as the exponential of a sum of weighted integrals would be desirable. Introducing the effective illuminated surface

$$S(t_1, r') = \int G^2(t_1, \mathbf{x}) \, \chi^2(r' - r(t_1, \mathbf{x})) dS, \tag{A8}$$

5   the normalized weighting function

$$W(t_1, r', \mathbf{x}) = \frac{G^2(t_1, \mathbf{x}) \, \chi^2(r' - r(t_1, \mathbf{x}))}{S(t_1, r')}, \tag{A9}$$

the average and fluctuating parts of the NRCS

$$\overline{\sigma^0}(t_1, r') = \int W(t_1, r', \mathbf{x}) \sigma^0(t_1, \mathbf{x}) dS, \tag{A10}$$

$$\widetilde{\sigma^0}(t_1, r', \mathbf{x}) = \frac{\sigma^0(t_1, \mathbf{x})}{\overline{\sigma^0}(t_1, r')}, \tag{A11}$$

and borrowing the algebraic technique of "cumulant expansion" from probability theory, it is possible to express $PP_{\Delta t}$ as

$$PP_{\Delta t}(t_1, r') = \frac{A^2(r')}{r'^4} \times \gamma_{TS}(\Delta t) \times \overline{\sigma^0}(t_1, r') \times S(t_1, r') \times \exp\left[\sum_{n=1}^{\infty} \frac{(i2k\Delta t)^n}{n!} \kappa_n\right], \tag{A12}$$

with κ_n the successive "cumulants" of $\mathbf{e}(\mathbf{x}) \cdot (\mathbf{V}_R - \mathbf{v}_s(\mathbf{x}))$ with respect to the "density distribution" $\widetilde{\sigma^0}(t_1, r', \mathbf{x}) W(t_1, r', \mathbf{x})$. As all the κ_n are real, we see that odd-n terms contribute to the argument of the pulse-pair signal, while even-n terms contribute to its magnitude. Keeping only the first two terms in the sum, one obtains:

15   $$PP_{\Delta t}(t_1, r') = \frac{A^2(r')}{r'^4} \times \gamma_{TS}(\Delta t) \times \overline{\sigma^0}(t_1, r') \times S(t_1, r') \times \exp\left[i2k\Delta t\kappa_1\right] \times \exp\left[-2(k\Delta t)^2\kappa_2\right]. \tag{A13}$$

As expected, the expression of κ_1,

$$\kappa_1(t_1, r') = \int W(t_1, r', \mathbf{x}) \, \widetilde{\sigma^0}(t_1, r', \mathbf{x}) \, \mathbf{e}(\mathbf{x}) \cdot (\mathbf{V}_R - \mathbf{v}_s(\mathbf{x})) \, dS \tag{A14}$$

shows that to first order the argument of the pulse-pair signal gives access to the integral over the footprint of the relative velocity of the scatterers with respect to the radar. The expression of κ_2,

20   $$\kappa_2(t_1, r') = \int W(t_1, r', \mathbf{x}) \, \widetilde{\sigma^0}(t_1, r', \mathbf{x}) \, [\mathbf{e}(\mathbf{x}) \cdot (\mathbf{V}_R - \mathbf{v}_s(\mathbf{x})) - \kappa_1]^2 \, dS, \tag{A15}$$

is a description of the impact of the variability of $\mathbf{e}(\mathbf{x})$, $\widetilde{\sigma^0}$ and $\mathbf{v}_s$ inside the footprint on the pulse-pair signal magnitude.

A1.4   Pulse-pair signal phase approximation

Working now in the Earth-fixed referenced frame at the observation point, we define

$$V_{\text{GD}} = -\int W(t_1, r', \mathbf{x}) \, \widetilde{\sigma^0}(t_1, r', \mathbf{x}) \, \mathbf{e}(\mathbf{x}) \cdot \mathbf{v}_s(\mathbf{x}) \, dS \tag{A16}$$

the (geophysically relevant) weighted projection of the scatterers velocity in that frame on the radar line-of-sight and

$$V_{\mathrm{NG}}(t_1, r') = \mathbf{V}_R \cdot \int W(t_1, r', \mathbf{x}) \, \widetilde{\sigma^0}(t_1, r', \mathbf{x}) \, \mathbf{e}(\mathbf{x}) \, dS \tag{A17}$$

the (non-geophysical) projection of the radar velocity. (Our conventions are such that V_{GD} is positive when the scatterers move towards the radar, and that V_{NG} is positive when the radar moves towards the footprint, in keeping with everyday intuition).

5   With these conventions, one sees that:

$$V_{\mathrm{GD}}(t_1, r') = \kappa_1(t_1, r') - V_{\mathrm{NG}}(t_1, r'). \tag{A18}$$

Using equation (A13), one can obtain κ_1 approximately as $1/(2k\Delta t)$ times the argument of the complex pulse-pair signal. At this stage, one must however consider a bit carefully the ambiguity that is inherent in phase measurements. As the phase of a complex number is only known up to a multiple of 2π, κ_1 is only obtained up to a multiple of $\frac{\lambda}{2\Delta t}$. This effect can be
10   neglected as long as both V_{NG} and κ_1 remain within the unambiguous interval $\left[-\frac{\lambda}{4\Delta t}; \frac{\lambda}{4\Delta t}\right]$. For larger platform velocities, care must be taken to add the right multiple of $\frac{\lambda}{2\Delta t}$ to κ_1 before subtracting V_{NG}. For airborne instruments it is usually feasible to select a small enough PRI to avoid ambiguity altogether. For satellite instruments, one approach is to select a solid Earth fixed reference frame, in which $\mathbf{v}_s$ is small, and to work on the phase-migrated pulse pair signal

$$\widetilde{PP}_{\Delta t}(t_1, r') = \exp\left[-\mathrm{i}2k\Delta t V_{\mathrm{NG}}\right] \times PP_{\Delta t}(t_1, r'). \tag{A19}$$

15   It is easy to see that V_{GD} can be retrieved as

$$V_{\mathrm{GD}}(t_1, r') = \frac{1}{2k\Delta t} \arg\left(\widetilde{PP}_{\Delta t}(t_1, r')\right). \tag{A20}$$

At this stage, even a coarse approximation of V_{NG} can be used, as long as it is sufficient to resolve the phase ambiguity. This is important in particular for the onboard processors of satellite instruments, which have to rely on limited quality position/velocity/pointing information and typically can not use the $\widetilde{\sigma^0}$ distribution information ground segment processors can
20   retrieve from the signal. The correction applied by the onboard processor must however be accounted for in later processing stages.

A2   Non-geophysical contribution V_{NG}

The Non-Geophysical contribution V_{NG} must be estimated from the platform velocity and radar beam pointing. For pulse-limited instruments such as KuROS and SKaR, the incidence angle is determined in each range bin as a function of the altitude.
25   The accuracies of the range resolution and altitude determination processes are then critical. Last, asymmetric azimuthal variation of the sea surface NRCS within a given range bin tend to bias the effective observation azimuth towards the brighter part of the instrument FOV. This section discusses these different aspects.

A2.1   Beam pointing accuracy

From now on, we work in the simplified setting of the flat-Earth approximation, in which the elevation and incidence angles
30   γ and θ are equal. We use a platform-fixed reference frame, the origin of which is located at the antenna phase center of the

instrument, with x-vector pointing to the geometric front of the platform, y-vector pointing to starboard, and z-vector pointing to the floor, and a local geographic North/East/Down reference frame, the origin of which is fixed to the solid Earth and located at a suitable point of the campaign area.

The orientation of the platform-fixed reference frame with respect to the local geographic frame is provided by the platform IMU as (Roll, Pitch, Heading) Euler angles, from which one can construct the Direction Cosine Matrix

$$\mathbf{DCM} = \begin{bmatrix} c_p.c_h & s_r.s_p.c_h - c_r.s_h & c_r.s_p.c_h + s_r.s_h \\ c_p.s_h & s_r.s_p.s_h + c_r.c_h & c_r.s_p.s_h - s_r.c_h \\ -s_p & s_r.c_p & c_r.c_p \end{bmatrix} \tag{A21}$$

allowing one to express the components of a vector in the (N, E, D) frame from its (x, y, z) components in the platform-fixed frame. The two reference frames are consistent in the sense that the frame vectors coincide when the platform is in constant altitude flight towards the North. In the above expression we have used the transparent notation $c_p \to \cos(\text{pitch}), s_r \to \sin(\text{roll}), c_h \to \cos(\text{heading})$, etc... Other quantities worth introducing are the course c and glide angle g such that the plane velocity vector in the NED frame is

$$\mathbf{V}_R = V_R \left[\cos(g)\cos(c)\mathbf{N} + \cos(g)\sin(c)\mathbf{E} + sin(g)\mathbf{D}\right]. \tag{A22}$$

In the NED frame, the pointing vector $\mathbf{e}$ can be expressed as

$$\mathbf{e} = \sin(\theta)\left[\cos(\varphi)\mathbf{N} + \sin(\varphi)\mathbf{E}\right] + \cos(\theta)\mathbf{D}. \tag{A23}$$

Its components in the platform-fixed frame can be determined using the fact that $\mathbf{DCM}^{-1} = \mathbf{DCM}^T$. The corresponding antenna azimuth and elevation angles φ and γ, in terms of which the radiation diagram is specified, can then be expressed using the platform-fixed to antenna-fixed reference frame transformation matrix.

With these notations, and using eq. (A17), one can express V_{NG} as

$$V_{NG}(t_1, r') = V_R \int W(t_1, r', \mathbf{x}) \, \widetilde{\sigma^0}(t_1, r', \mathbf{x}) \, \left[\cos(g)\sin(\theta)\cos(\varphi - c) + \sin(g)\cos(\theta)\right] \, dS. \tag{A24}$$

Constant altitude flight corresponds to $g \simeq 0$. We thus concentrate on the impact of errors in the first term of the RHS of this equation. Quite clearly, the impact of errors in $\sin(\theta)$ is largest when the instrument views the area where $\cos(\varphi - c)$ is large, *i.e* in the up/down-track directions, while the impact of errors in the azimuthal direction is largest when the instrument looks cross-track (i.e. where the derivative of $\cos(\varphi - c)$ is close to 1).

Leaving aside for the moment the effects of uncertainties on $W(t_1, r', \mathbf{x})$ and $\widetilde{\sigma^0}(t_1, r', \mathbf{x})$, one sees that at 12° incidence angle, and for a platform velocity of 7000 m/s (space-borne instrument), the SKIM 40 cm/s error budget on horizontal velocity measurements translates to pointing accuracies of 4.5 and 21 microradians in incidence angle and azimuth, respectively (see the discussion in section 2.3). In the airborne case at 120 m/s platform velocity and 3000 m altitude, the corresponding numbers are 0.26 and 1.25 milliradians for incidence angle and azimuth pointing accuracy for KuROS, respectively. In the cross-track viewing geometry of KaRADOC, only the comparatively mild (but still quite demanding) 1.25 milliradians azimuth pointing accuracy requirement applies.

(A)
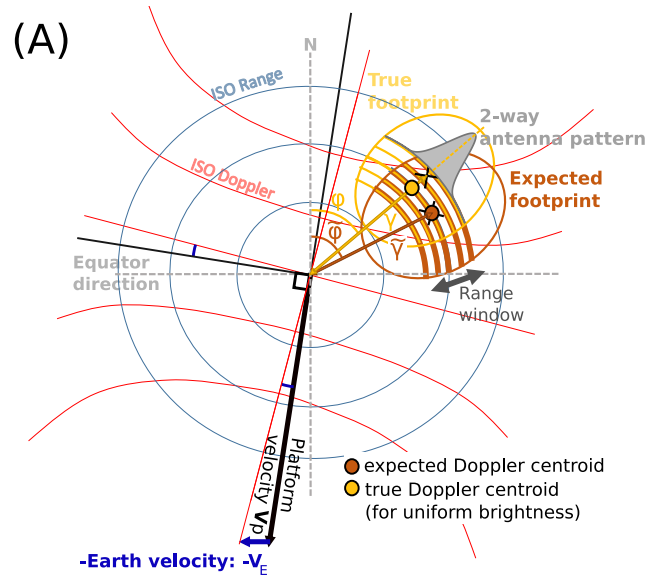
(B) Antenna pattern and 100x distortions due to brightness gradients across footprint
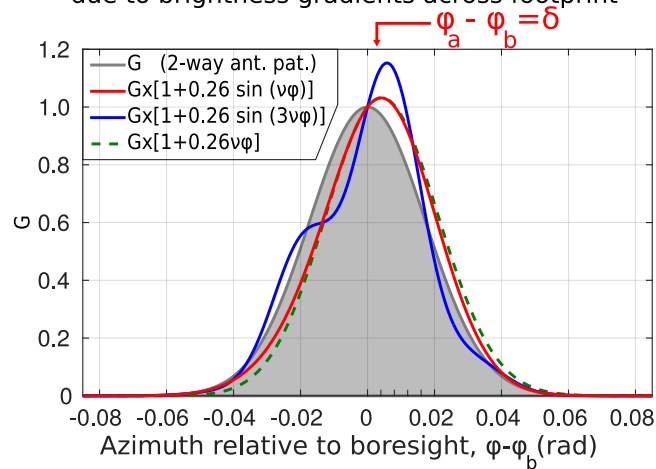
Figure A1. (A) True pointing. The attitude drift changes the antenna footprint direction and shifts the DFS centroid. Here (γ, φ) are the expected coordinate of the antenna gain ground projection while $(\tilde{\gamma}, \tilde{\varphi})$ are the shifted version of these coordinates by the attitude misknowledge (adapted from Delouis *et al.*). (B) Apparent pointing φ_a for the SKIM geometry. Examples of 2-way antenna gain G as a function of azimuth and distortions (exaggerated 100 times) induced by σ^0 gradients on the power integrated by the radar in the azimuth direction across the antenna diagram (grey curve). Three examples of asymmetric distortions are given: a sine function with $\nu = \sin\theta / \sigma_\alpha$, a 3-times faster varying sine function, and a linear trend. Such distortions induce an apparent mispointing of the beam $\delta\varphi$, and a correction to the geometrical line-of-sight relative velocity estimate.

Figure (A1.A) shows the measurement geometry, seen from above. One can see that uncertainties on the viewing azimuth and incidence angle have different origins:

– the uncertainty in azimuth can be due to an imperfect knowledge of the weighting corresponding to the $W(t_1, r', \mathbf{x}) \, \widetilde{\sigma^0}(t_1, r', \mathbf{x})$ term in eq. (A24). This can of course come from imperfect platform attitude or antenna orientation information, but also from an imperfect characterization of the antenna radiation diagram or of the distribution of σ^0 on the sea surface.

– the uncertainty in incidence angle is due to an imperfect knowledge of the radial position of the range resolution bins (yellow striping of the footprint in fig. A1.A). This can be due to an imperfect timing accuracy, or to an imperfect knowledge of the vertical separation between the instrument and sea surface.

A2.2 Timing and altitude accuracy

For this brief discussion of the effects of timing and altitude accuracy on incidence angle estimation, we consider a single range bin whose "true" range from the radar is r, whose altitude with respect to the radar is H, and where the incidence angle is θ. In this case $\theta = \arccos(H/r)$. If now the radar suffers from a timing error δr, the instrument will detect a false altitude $H - \delta r$, but will ascribe to range bin $r - \delta r$ the signal coming from r. In the meantime, we consider that the surface-tracking algorithm suffers from an error δh, and detects the surface at range $H - \delta r - \delta h$. The data from this range bin will thus be processed using an angle of incidence

$$\theta + \delta\theta = \arccos\left(\frac{H - \delta r - \delta h}{r - \delta r}\right), \tag{A25}$$

different from the correct value by

$$\delta\theta \simeq \frac{1}{H \tan(\theta)} \left[\delta h + \delta r \left[1 - \cos(\theta)\right]\right]. \tag{A26}$$

Considering δh and δr as independent, we see that at 12° the incidence angle knowledge requirements expressed above for SKIM and KuROS translate respectively to timing accuracy requirements of 36.8 m and 7.7 m, and to surface-tracking accuracy requirements of 80.4 cm and 16.9 cm.

The timing accuracy requirements are easily met in the spaceborne context, but can be challenging in the cost-constrained context of an airborne instrument.

The surface-tracking algorithm, however, does not benefit from the error-compensation that exists for the timing error. The requirement for SKIM is easily met by the nadir altimeter payload of SKIM. The 80.4 cm altitude tracking requirement is out of reach of the KuROS airborne instrument. Our analysis of its DFS data will thus be restricted to the side-looking configurations for which, as per eq. (A24), the pointing requirements are much milder.

A2.3 Effective pointing / Azimuth Gradient DFS

As expressed in eq. (A24), for each range resolution cell V_{NG} results from an integral over azimuth with a weight that depends on the product of the antenna radiation diagram and the sea surface NRCS, which varies as a function of the horizontal position

(x, y) due to the presence of waves, varying winds, currents, surfactants, sea ice and all the physical properties of the sea surface.

Even with a perfect knowledge of the platform attitude and velocity, NRCS variations can thus make the effective pointing of the measurements deviate from the pure geometric estimates. Valuable insight into this effect can be gained by considering the saddle-point approximation of eq. (A24) in the limit of a very narrow antenna diagram (which is clearly applicable for SKIM and KaRADOC, less so for KuROS).

Considering first the case of an antenna pointing towards azimuth φ_b with an infinitely narrow radiation diagram, we see that the product $W(t_1, r', \varphi) \widetilde{\sigma^0}(t_1, r', \varphi)$ is well approximated by the Dirac distribution $\delta(\varphi - \varphi_b)$. In this limit

$$V_{NG}(t_1, r') = V_R \left[\cos(g) \sin(\theta) \cos(\varphi_b - c) + \sin(g) \cos(\theta) \right]. \tag{A27}$$

We recognize in this expression V_{geo}, the estimate of V_{NG} one would have derived using direct geometric arguments.

The essence of the argument is that the sharpest factor in the integral is the beam radiation diagram. If it is now not infinitely sharp, we see that the effet of a gradient of $\widetilde{\sigma^0}$ is to shift the peak of the distribution by an angle

$$\delta\varphi = -\frac{\partial_\varphi \log(\widetilde{\sigma^0})\big|_{\varphi_b}}{\partial_{\varphi\varphi} \log(W)\big|_{\varphi_b}}. \tag{A28}$$

Assuming for $W(t_1, t', \varphi)$ a Gaussian approximation

$$W(t_1, r', \varphi) = \frac{1}{\sqrt{\pi}\sigma_\varphi(r')} \exp\left[-\frac{(\varphi - \varphi_b)^2}{\sigma_\varphi^2(r')} \right] \tag{A29}$$

in which $\sigma_\varphi(r')$ is a parameter describing the width of the antenna diagram at the working incidence angle, one obtains

$$V_{NG}(t_1, r') = V_R \left[\cos(g) \sin(\theta) \cos(\varphi_b - c + \delta\varphi) + \sin(g) \cos(\theta) \right]. \tag{A30}$$

with

$$\delta\varphi = \frac{\sigma_\varphi^2(r')}{2} \partial_\varphi \log(\widetilde{\sigma^0}). \tag{A31}$$

Alternatively, one can choose to express V_{NG} as the sum of V_{geo}, the geometric approximation, plus an Azimuth Gradient Doppler velocity contribution

$$V_{NG}(t_1, r') = V_{geo}(t_1, r') + V_{AGD}(t_1, r'), \tag{A32}$$

with

$$V_{geo}(t_1, r') = V_R \left[\cos(g) \sin(\theta) \cos(\varphi_b - c) + \sin(g) \cos(\theta) \right] \tag{A33}$$

and

$$V_{AGD}(t_1, r') = -V_R \cos(g) \sin(\theta) \sin(\varphi_b - c) \frac{\sigma_\varphi^2(r')}{2} \partial_\varphi \log(\widetilde{\sigma^0}). \tag{A34}$$

One can see from these expressions that for a given azimuthal variation of the NRCS the order of magnitude of V_{AGD} is set by the width of the antenna radiation diagram: instruments with a thin diagram, such as SKIM and KaRADOC, are less affected than instruments with a broader diagram, such as KuROS. Also, one sees that V_{AGD} is largest when the instrument looks in the cross-track direction, and is zero in the up/down track viewing directions. Finally, one sees that V_{AGD} is equivalent to the line-of-sight projection of a spurious horizontal velocity U_{AGD}, which varies with incidence angle only through the variations of $\widetilde{\sigma^0}$ and σ_φ:

$$U_{AGD}(t_1, r') = -V_R \sin(\varphi_b - c)\frac{\sigma_\varphi^2(r')}{2}\partial_\varphi \log(\widetilde{\sigma^0}). \tag{A35}$$

At small scales, spatial gradients add to the azimuthal gradient and also induce a spurious velocity with the same expression as a function of $\widetilde{\sigma^0}$. Using the simple case of a single Fourier component $\widetilde{\sigma^0} = \varepsilon \sin[\nu(\varphi - \varphi_b)]$ allows one to evaluate the importance of different scales. The azimuthal shift can be obtained as

$$\delta\varphi = \varepsilon \exp\left(-\frac{(\nu^2 + 1)\sigma_\varphi^2}{4}\right)\sinh\left(\frac{\nu\sigma_\varphi^2}{2}\right). \tag{A36}$$

In the slow-variation limit $\nu, \sigma_\varphi \to 0$, and eq. (A36) this expression coincides with eq. (A31). For faster variations, one sees that the largest disturbance is obtained when $\nu \sim \sqrt{2}/\sigma_\varphi$. This azimuthal wavenumber is such that the footprint can host a bright and a dark patch, one on either side of the look direction. This configuration creates the largest disturbance for a given value of the brightness contrast ε. $\delta\varphi$ in this case is given by

$$\delta\varphi_{\max} = \varepsilon\sigma_\varphi e^{-1/2}/\sqrt{2}. \tag{A37}$$

Appendix B: KuROS antenna diagram determination

A precise determination of the antenna diagram is necessary for any Doppler application, given the possibly large contribution of pointing errors $\varphi_b - \widetilde{\varphi}$ in the estimation of the non-geophysical DFS, and the effect of the antenna beamwidth in the spurious Azimuth Gradient velocity U_{AGD}. A comprehensive strategy has thus been developed for estimating the 1-way antenna diagram in amplitude and phase, combining anechoic chamber measurements and verification using the campaign data, and final adjustment of systematic phase shifts in the data. (In this section α and β are respectively the latitude and longitude of a set of spherical coordinates centered on the antenna, and such that the main lobe extends in a longitudinal sector on the equator $\alpha = 0°$, and the rotation axis of the antenna turntable points towards $\alpha = 0°$, $\beta = 0°$. With this choice of coordinates the antenna diagram has separable Gaussian dependencies on α and β. In constant altitude flight, when the antenna points towards φ_b, $\sin(\alpha) = \sin(\theta)\sin(\varphi - \varphi_b)$, $\tan(\beta) = \tan(\theta)\cos(\varphi - \varphi_b)$).

B1   Fixed antenna NRCS correction

The anechoic chamber measurements are very accurate for the antenna alone. However, once integrated into the plane, the antenna diagram is perturbed. This is for instance particularly noticeable in the NRCS measurements in rotating mode, where

a spurious azimuthal pattern could clearly be seen, or for fixed-antenna DFS observations, where a "striping" pattern as a function of incidence angle is obvious. We have thus developed a complementary method that relies on the variations of the
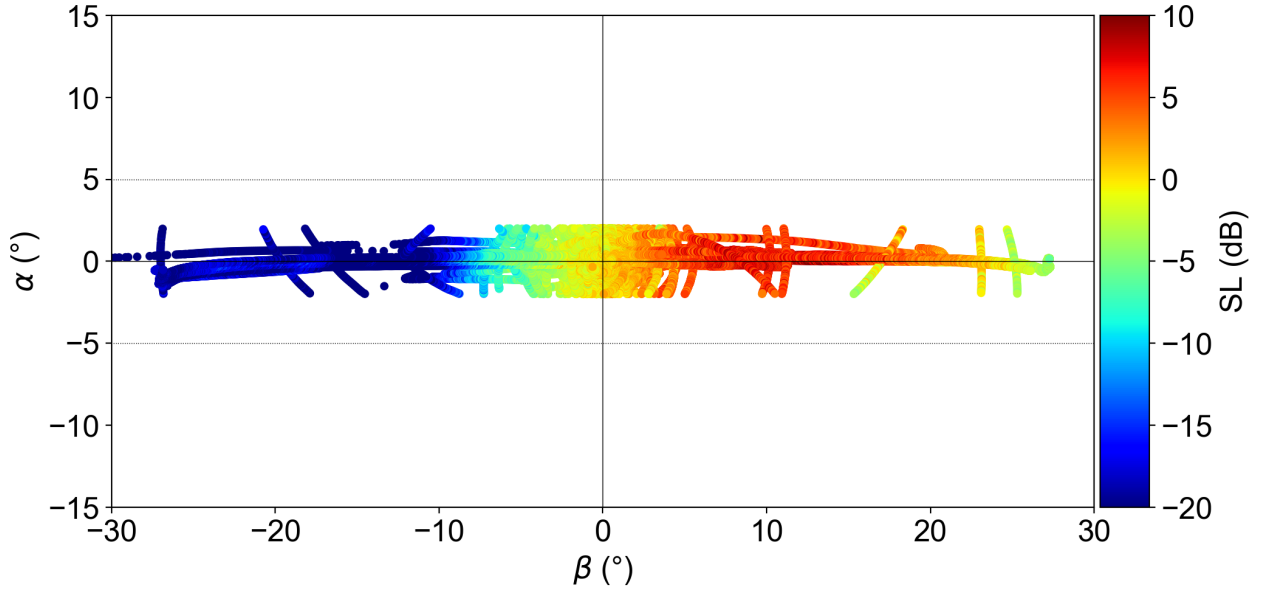
Figure B1. Reconstructed α, β dependence of the 2-way KuROS antenna diagram. For each 30 s data segment, the constant altitude values, for which the nadir is at $\alpha = 0$, $\beta = 0$, have been used as reference level to account for geophysical variations in nadir NRCS.

plane attitude during maneuvers. Using the plane IMU, we identify the angular coordinates α and β of the nadir, and use the measured power to map the antenna diagram (using as a reference point the constant altitude return power values for each data
5 segment, to account for geophysical nadir NRCS variations). The combination of all the flights during the campaign gives the distribution of measured power as a function of α and β that is shown in Figs. B1 and B2.

The measured distribution is well approximated by a Gaussian shape

$$G(\alpha, \beta) = \exp\left[-\frac{\alpha^2}{2\sigma_\alpha^2} - \frac{(\beta - \beta_0)^2}{2\sigma_\beta^2}\right]. \tag{B1}$$

Another expression for $G(\alpha, \beta)$, more suitable for use with the half-power beamwidths $\alpha_{-3\mathrm{dB}}$ and $\beta_{-3\mathrm{dB}}$ obtained from
10 anechoic chamber measurements, is:

$$G(\alpha, \beta) = 2^{\left[-\frac{4\alpha^2}{\alpha_{-3\mathrm{dB}}^2} - \frac{4(\beta - \beta_0)^2}{\beta_{-3\mathrm{dB}}^2}\right]}. \tag{B2}$$

The width parameters in these equations are linked by

$$\sigma_\alpha = \alpha_{-3\mathrm{dB}}/\sqrt{8\log(2)}, \; \sigma_\beta = \beta_{-3\mathrm{dB}}/\sqrt{8\log(2)} \tag{B3}$$

The parameter values used in this study are collected in table 1.

One cautionary remark is that the illuminated patch at nadir is not infinitely sharp. The measured distribution is thus the convolution of the true antenna diagram by the power distribution at the nadir patch (which depends on the altitude tracking error as well as the sea state (Chelton et al., 1989)). Assuming Gaussian shapes, the squares of the width parameters add, leading to

$$\sigma_{observed} \simeq \sigma_{true} \left[1 + \frac{\sigma_{patch}^2}{2\sigma_{true}^2} \right].$$

(B4)

The broadening of the diagram due to finite nadir patch size is thus a small correction provided the scale of the nadir patch remains smaller than the antenna diagram scales. For reasonable orders of magnitude of the altitude tracking error and significant wave height, the patch -3 dB width is of the order of 3° when viewed from 3000 m height. This corresponds to a 3% correction on the value of σ_α. We have chosen to neglect this correction. The values summarized in table 1 are the parameters of the Gaussian fits to the observed distributions.

B2   Rotating antenna NRCS correction

Using these parameters as a starting point, we have then constructed corrections for the rotating antenna measurements of NRCS, by allowing the boresight elevation β_0 to vary as a function of antenna orientation within the plane. The variation law was determined by minimizing the dependence of the rotating-antenna NRCS measurements as a function of flight direction over the "offshore" area for each day.

B3   Fixed antenna DFS correction

In a similar way, we have observed that the KuROS antenna diagram is slightly "wrinkled", in that the beam boresight azimuth changes as a function of elevation. This azimuthal mispointing transposes immediately into a striping modulation of the U_{GD} estimates. A correction was introduced by allowing the boresight azimuth α_0 to vary as a function of β. The variation law of α_0 was determined by minimizing the average U_{GD} over all flights for each value of β. As the variation of this quantity with respect to $\alpha_0(\beta)$ is not trivial, this required constructing, regularizing and inverting the observation matrix.

Appendix C: KaRADOC system

KaRADOC is built around an Agilent PNA-X network analyzer, complemented by a TX power amplifier, a T/R switch, a RX low-noise amplifier, and a high-gain purpose-built slotted waveguide antenna (shown in Fig. C1).

The beam can be steered in elevation by changing the instrument working frequency (see Fig. C2A), and the antenna is usually mounted on a pitch/roll stabilization platform. For the Drift4SKIM experiment, however, the antenna was rigidly mounted in a port-looking configuration, centered on 10° incidence angle, with a 2° backward-looking tilt to compensate for the aircraft pitch in constant altitude flight. Plane attitude variations were accounted for in the data processing. Observations
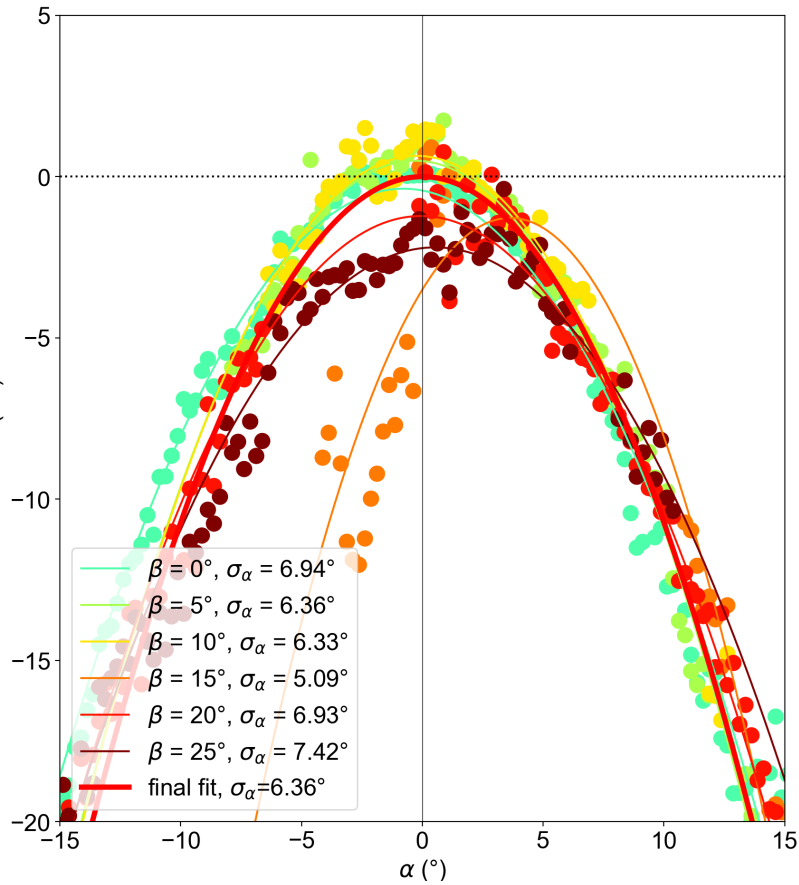
Figure B2. Reconstructed azimuth dependence of nadir return power for different incidence angles. For each incidence angle, the $\alpha = 0$ value has been used as a reference. The thick line shows the final Gaussian fit used in the data analysis. The $\beta = 15^o$ data were excluded from the fit.

were collected at 33.7 GHz, corresponding to $12°$ nominal incidence angle. Other angles were also scanned, but RF leakage from the TX to the RX subsystems was too strong at the corresponding frequencies, making the signal harder to analyze.

The antenna radiation diagram is very narrow, with a beamwidth less than $1.5°$ in elevation and less than $2°$ in azimuth (see Fig. C2B). Figures C3A and C3B) represent sections across the KaRADOC main lobe in the azimuth and elevation direction, at 33.7 GHz.
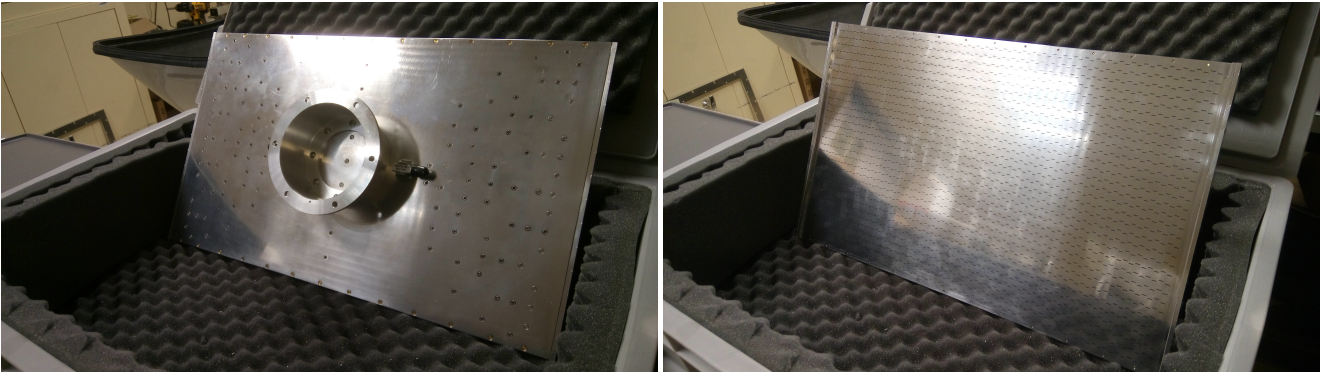
Figure C1. The back (on the left) and the front (on the right) of the antenna
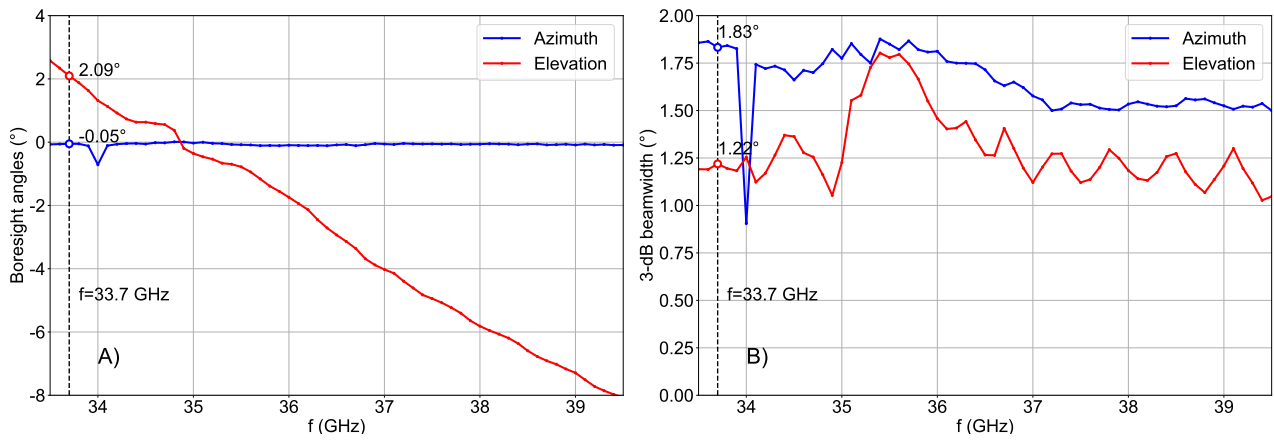
Figure C2. Frequency dependence of the KaRADOC main lobe azimuth and elevation boresight angles (A) and half-power beamwidths (B).
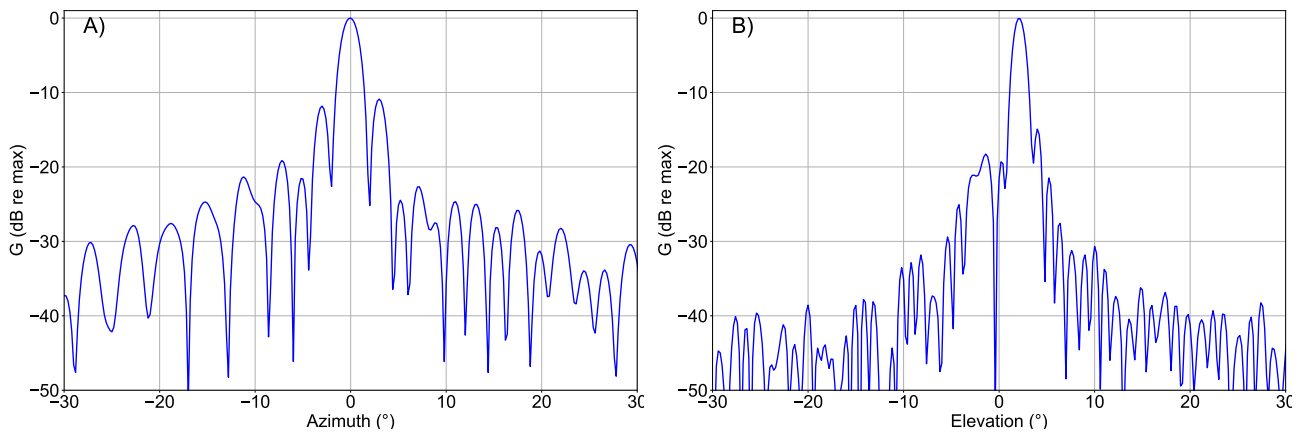
Figure C3. KaRADOC radiation diagram at 33.7 GHz as a function of (A) azimuth at 2.09° elevation and (B) elevation at -0.05° azimuth.

Author contributions. All authors have contributed to the writing of the paper..

Competing interests. The authors declare that they have no conflict of interest.

Disclaimer. The views and opinions expressed in this publication can in no way be taken to reflect the official opinion of the European Space Agency.

Acknowledgements. This study was supported by the KuROS4SKIM, DRIFT4SKIM and IASCO contracts from the European Space Agency, made possible by the unflagging determination of Erik de Witte. The in situ measurements owe much to the dedication of the R/V Thalia crew. Airborne data were obtained using the aircraft managed by Safire, the French facility for airborne research, an infrastructure of the French National Center for Scientific Research (CNRS), Météo-France and the French National Center for Space Studies (CNES). Many people at LOPS and OceanDataLab also contributed to the preparation, deployment and recovery of the instruments, including Mickael Accensi, Sylvain Herledan, Gilles Guitton, Lucile Gaultier, Michel Hamon, Olivier Péden, Stéphane Leizour, Pierre Branellec. Many people at IETR are involved in the KaRADOC developments: Cécile Leconte, Mohamed Himdi, Paul Leroy, Eric Pottier and especially Guy Grunfelder and Mor Diama Lo who have made possible the measurement campaign during November, 2018. Operation of KuROS during the experiment would not have been possible without the dedication of Christophe Le Gac, Nicolas Pauwels and Christophe Dufour, from CNRS/LATMOS.

References

Ardhuin, F., Marié, L., Rascle, N., Forget, P., and Roland, A.: Observation and estimation of Lagrangian, Stokes and Eulerian currents induced by wind and waves at the sea surface, J. Phys. Oceanogr., 39, 2820–2838, doi:10.1175/2009JPO4169.1, http://journals.ametsoc.org/doi/pdf/10.1175/2009JPO4169.1, 2009.

5 Ardhuin, F., Balanche, A., Stutzmann, E., and Obrebski, M.: From seismic noise to ocean wave parameters: general methods and validation, J. Geophys. Res., 117, C05 002, doi:10.1029/2011JC007449, 2012.

Ardhuin, F., Aksenov, Y., Benetazzo, A., Bertino, L., Brandt, P., Caubet, E., Chapron, B., Collard, F., Cravatte, S., Dias, F., Dibarboure, G., Gaultier, L., Johannessen, J., Korosov, A., Manucharyan, G., Menemenlis, D., Menendez, M., Monnier, G., Mouche, A., Nouguier, F., Nurser, G., Rampal, P., Reniers, A., Rodriguez, E., Stopa, J., Tison, C., Tissier, M., Ubelmann, C., van Sebille, E., Vialard, J., and Xie, J.:

10 Measuring currents, ice drift, and waves from space: the Sea Surface KInematics Multiscale monitoring (SKIM) concept, Ocean Sci., 14, 337–354, doi:10.5194/os-2017-65, 2018.

Ardhuin, F., Chapron, B., Maes, C., Romeiser, R., Gommenginger, C., Cravatte, S., Morrow, R., Donlon, C., and Bourassa, M.: Satellite Doppler observations for the motions of the oceans, Bull. Amer. Meterol. Soc., 100, doi:10.1175/BAMS-D-19-0039.1, 2019.

Barrick, D. E., Headrick, J. M., Bogle, R. W., and Crombie, D. D.: Sea backscatter at HF: interpretation and utilization of the echo, Proc.

15 IEEE, 62, 673, 1974.

Beckmann, P. and Spizzichino, A.: The scattering of electromagnetic waves from rough surfaces, Artech House, Norwood, MA, USA, 1987.

Benoit, M., Frigaard, P., and Schäffer, H. A.: Analysing multidirectional wave spectra: a tentative classification of available methods, in: Proceedings of the 1997 IAHR conference, San Francisco, pp. 131–158, The Johns Hopkins University Press, Baltimore, 1997.

Buck, C.: An extension to the wide swath ocean altimeter concept, in: Proceedings of the IEEE International Geoscience and Remote Sensing

20 Symposium (IGARSS), 2005., vol. 8, pp. 543–5439, IEEE, doi:10.1109/IGARSS.2005.1525970, 2005.

Caudal, G., Hauser, D., Valentin, R., and Gac, C. L.: KuROS: A new airborne Ku-band doppler radar for observation of surfaces, J. Atmos. Ocean Technol., 31, 2023–2245, doi:10.1175/JTECH-D-14-00013.1, 2014.

Chapron, B., Vandemark, D., and Elfouhaily, T.: On the skewness of the sea slope probability distribution, in: Gas transfer at water surfaces, edited by Donelan, M. A., Drennan, W. M., Saltzman, E. S., and Wanninkhof, R., vol. 127 of *Geophys. Monogr. Ser.*, pp. 59–63, American

25 Geophysical Union, doi:10.1029/GM127p0059, 2002.

Chapron, B., Collard, F., and Ardhuin, F.: Direct measurements of ocean surface velocity from space: interpretation and validation, J. Geophys. Res., 110, doi:10.1029/2004JC002809, 2005.

Chelton, D. B., Walsh, E. J., and MacArthur, J. L.: Pulse compression and sea level tracking in satellite altimetry, J. Atmos. Ocean Technol., 6, 407–438, doi:10.1175/1520-0426(1989)006<0407:pcaslt>2.0.co;2, 1989.

30 Chelton, D. B., Schlax, M. G., Samelson, R. M., Farrar, J. T., Molemaker, M. J., and Gula, J. C. M. J.: Prospects for future satellite estimation of small-scale variability of ocean surface velocity and vorticity, Progress in Oceanography, 173, 256–350, doi:10.1016/j.pocean.2018.10.012, 2019.

Chu, X., He, Y., and Chen, G.: Asymmetry and anisotropy of microwave backscatter at low incidence angles, IEEE Transactions on Geoscience and Remote Sensing, 50, 4014–4024, 2012.

35 Crombie, D. D.: Theory of HF ground wave backscatter from sea waves, Nature, 175, 681–682, 1955.

Elfouhaily, T., Chapron, B., Katsaros, K., and Vandemark, D.: A unified directional spectrum for long and short wind-driven waves, J. Geophys. Res., 102, 15 781–15 796, doi:10.1029/97jc00467, 1997.

Elfouhaily, T. M.: A consistent wind and wave model and its application to microwave remote sensing of the ocean surface, Ph.D. thesis, Denis Diderot University, Paris, 1997.

ESA: Report for Mission Selection: SKIM, Tech. Rep. ESA-EOPSM-SKIM-RP-3550, European Space Agency, Noordwijk, The Netherlands, doi:10.13140/RG.2.2.22907.98081/3, 2019.

Guimaraes, P. V., Ardhuin, F., Sutherland, P., Accensi, M., Hamon, M., Pérignon, Y., Thomson, J., Benetazzo, A., and Ferrant, P.: A Surface KInematics Buoy (SKIB) for wave-current interactions studies, Ocean Sci., doi:10.5194/os-2018-45, 2018.

Gurgel, K.-W., Antonischki, G., Essen, H.-H., and Schlick, T.: Wellen Radar (WERA), a new ground-wave based HF radar for ocean remote sensing, Coastal Eng., 37, 219–234, doi:10.1016/S0378-3839(99)00027-7, 1999.

Hansen, M. W., Johannessen, J. A., Dagestad, K. F., Collard, F., and Chapron, B.: Monitoring the surface inflow of Atlantic Water to the Norwegian Sea using Envisat ASAR, J. Geophys. Res., 116, C12 008, doi:10.1029/2011JC007375, 2011.

Hauser, D., Tison, C., Amiot, T., Delaye, L., Corcoral, N., and Castillan, P.: SWIM: The first spaceborne wave scatterometer, IEEE Trans. on Geosci. and Remote Sensing, 55, 3000–3014, 2017.

Hauser, D., Tourain, C., Hermozo, L., Alraddawi, D., Aouf, L., Chapron, B., Dalphinet, A., Delaye, L., Dalila, M., Dormy, E., Gouillon, F., Gressani, V., Grouazel, A., Guitton, G., Husson, R., Mironov, A., Mouche, A., Ollivier, A., Oruba, L., Piras, F., Suquet, R. R., Schippers, P., Tison, C., and Tran, N.: New Observations From the SWIM Radar On-Board CFOSAT: Instrument Validation and Ocean Wave Measurement Assessment, IEEE Transactions on Geoscience and Remote Sensing, pp. 1–22, doi:10.1109/TGRS.2020.2994372, 2020.

Jackson, F. C., Walton, W. T., and Baker, P. L.: Aircraft and satellite measurement of ocean wave directional spectra using scanning-beam microwave radars, J. Geophys. Res., 90, 987–1004, 1985.

Kenyon, K. E.: Stokes drift for random gravity waves, J. Geophys. Res., 74, 6991–6994, 1969.

Kirby, J. T. and Chen, T.-M.: Surface waves on vertically sheared flows: approximate dispersion relations, J. Geophys. Res., 94, 1013–1027, 1989.

Lazure, P. and Dumas, F.: An external-internal mode coupling for a 3D hydrodynamical model for applications at regional scale (MARS)., Adv. Water Resour., 31, 233–250, 2008.

Le Boyer, A., Cambon, G., Daniault, N., Herbette, S., Cann, B. L., Marié, L., and Morin, P.: Observations of the Ushant tidal front in September 2007, Continental Shelf Research, 29, 1026–1037, doi:10.1016/j.csr.2008.12.020, 2009.

LOPS: Estimation of non-geophysical Doppler and wave Doppler, and inversion algorithm for SKIM, Tech. Rep. SKIM-MPRC-TN5-V1.5-LOPS-2019, ESA, doi:10.13140/RG.2.2.22907.98081/3, 2019.

Lygre, A. and Krogstad, H. E.: Maximum entropy estimation of the directional distribution in ocean wave spectra, J. Phys. Oceanogr., 16, 2,052–2,060, 1986.

Martin, A. C. H., Gommenginger, C., Marquez, J., Doody, S., Navarro, V., and Buck, C.: Wind-wave-induced velocity in ATI SAR ocean surface currents: First experimental evidence from an airborne campaign, J. Geophys. Res., 121, 1640–1653, doi:10.1002/2015JC011459, 2016.

Martin, A. C. H., Gommenginger, C. P., and Quilfen, Y.: Simultaneous ocean surface current and wind vectors retrieval with squinted SAR interferometry: Geophysical inversion and performance assessment, Remote sensing of Environment, 216, 798–808, doi:10.1016/j.rse.2018.06.013, 2018.

Munk, W.: An inconvenient sea truth: spread, steepness, and skewness of surface slopes, Annu. Rev. Mar. Sci., 1, 377–415, doi:n10.1146/annurev.marine.010908.163940, 2008.

Niiler, P. P. and Paduan, J. D.: Wind-driven motions in the Northeast Pacific as measured by Lagrangian drifters, J. Phys. Oceanogr., 25, 2819–2930, http://ams.allenpress.com/archive/1520-0485/25/11/pdf/i1520-0485-25-11-2819, 1995.

Nouguier, F.: Remote Sensing Spatial Simulator (R3S), Tech. Rep. SKIM-MPRC-TN6-V1.0-LOPS-2019, ESA, 2019.

Nouguier, F., Guérin, C.-A., and Soriano, G.: Analytical techniques for the Doppler signature of sea surfaces in the microwave regime — I: linear surfaces, IEEE Trans. on Geosci. and Remote Sensing, 49, 4856–4864, doi:10.1109/TGRS.2011.2152848, 2011.

Nouguier, F., Mouche, A., Rascle, N., Chapron, B., and Vandemark, D.: Analysis of dual-frequency ocean backscatter measurements at Ku- and Ka-bands using near-nadir incidence GPM radar data, IEEE Geoscience And Remote Sensing Letters, 31, 2023–2245, doi:10.1109/LGRS.2016.2583198, 2016.

Nouguier, F., Chapron, B., Collard, F., Mouche, A., Rascle, N., Ardhuin, F., and Wu, X.: Sea surface kinematics from near-nadir radar measurements, IEEE Trans. on Geosci. and Remote Sensing, 56, 6169–6179, doi:10.1109/TGRS.2018.2833200, http://tiny.cc/SKIMonRG_NOUG, 2018.

Novelli, G., Guigand, C. M., Cousin, C., Ryan, E. H., Laxague, N. J. M., Dai, H., Haus, B. K., and Özgökmen, T. M.: A biodegradable surface drifter for ocean sampling on a massive scale, J. Atmos. Ocean Technol., 34, 2509–2532, doi:10.1175/JTECH-D-17-0055.1, 2017.

Peureux, C., Benetazzo, A., and Ardhuin, F.: Note on the directional properties of meter-scale gravity waves, Ocean Science, 14, 41–52, doi:10.5194/os-14-41-2018, 2018.

Raghukumar, K., Chang, G., Spada, F., Jones, C., Janssen, T., and Gans, A.: Performance characteristics of "Spotter," a newly developed real-time wave measurement buoy, Journal of Atmospheric and Oceanic Technology, 36, 1127–1141, doi:10.1175/JTECH-D-18-0151.1, https://doi.org/10.1175/JTECH-D-18-0151.1, 2019.

Redelsperger, J.-L., Bouin, M.-N., Pianezze, J., Garnier, V., and Marié, L.: Impact of a sharp, small-scale SST front on the marine atmospheric boundary layer on the Iroise Sea: Analysis from a hectometric simulation, Quarterly Journal of the Royal Meteorological Society, 145, 3692–3714, doi:10.1002/qj.3650, https://rmets.onlinelibrary.wiley.com/doi/abs/10.1002/qj.3650, 2019.

Rodriguez, E.: On the optimal design of Doppler scatterometers, Remote Sensing, 10, 1765, doi:doi:10.3390/rs10111765, 2018.

Rodríguez, E., Wineteer, A., Perkovic-Martin, D., Gál, T., Stiles, B. W., Niamsuwan, N., and Monje, R. R.: Estimating ocean vector winds and currents using a Ka-band pencil-beam Doppler scatterometer, Remote Sensing, 4, 576, doi:10.3390/rs10040576, 2018.

Roland, A. and Ardhuin, F.: On the developments of spectral wave models: numerics and parameterizations for the coastal ocean, Ocean Dynamics, 64, 833–846, doi:10.1007/s10236-014-0711-z, 2014.

Romeiser, R., Breit, H., Eineder, M., Runge, H., Flament, P., de Jong, K., and Vogelzang, J.: On the suitability of TerraSAR-X split antenna mode for current measurements by along-track interferometry, in: Proceedings of the IGARSS conference, Toulouse, France, 2003.

Rossby, T., Flagg, C. N., Donohue, K., Fontana, S., Curry, R., Andres, M., and Forsyth, J.: Oleander is more than a flower: twenty-five years of oceanography aboard a merchant vessel, Oceanography, 32, 126–137, doi:10.5670/oceanog.2019.319, https://doi.org/10.5670/oceanog.2019.319, 2019.

Rouault, M. J., Mouche, A., Collard, F., Johannessen, J. A., and Chapron, B.: Mapping the Agulhas Current from space: An assessment of ASAR surface current velocities, J. Geophys. Res., 115, C10 026, doi:10.1029/2009JC006050, 2010.

Sandwell, D. T. and Smith, W. H. F.: Slope correction for ocean radar altimetry., Journal of Geodesy, 88, 765–771, doi:10.1007/s00190-014-0720-1, 2014.

Stewart, R. H. and Joy, J. W.: HF radio measurements of surface currents, Deep Sea Res., 21, 1039–1049, 1974.

Stopa, J. E., Ardhuin, F., Bababin, A., and Zieger, S.: Comparison and validation of physical wave parameterizations in spectral wave models, Ocean Modelling, 103, 2–17, doi:10.1016/j.ocemod.2015.09.003, 2016.

Sudre, J., Maes, C., and Garçon, V.: On the global estimates of geostrophic and Ekman surface currents, Limnology and Oceanography: Fluids and Environments, 3, 1–20, doi:10.1215/21573689-2071927, 2013.

Sutherland, G., Marié, L., Reverdin, G., Christensen, K. H., Broström, G., and Ward, B.: Enhanced turbulence associated with the diurnal jet in the ocean surface boundary layer, J. Phys. Oceanogr., 46, 3051–3067, doi:10.1175/JPO-D-15-0172.1, 2016.

5 Sutherland, P., Brozena, J., Rogers, W. E., Doble, M., and Wadhams, P.: Airborne remote sensing of wave propagation in the marginal ice zone, Journal of Geophysical Research, 123, 4132–4152, doi:10.1029/2018JC013785, 2018.

Thomson, J., D'Asaro, E. A., Cronin, M. F., Rogers, W. E., Harcourt, R. R., and Shcherbina, A.: Waves and the equilibrium range at Ocean Weather Station P, J. Geophys. Res., 118, 595–5962, doi:10.1002/2013JC008837, 2013.

Walsh, E. J., Hancock, III, D. W., Hines, D. E., Swift, R. N., and Scott, J. F.: An observation of the directional wave spectrum evo-
10   lution from shoreline to fully developed, J. Phys. Oceanogr., 17, 1288–1295, http://ams.allenpress.com/archive/1520-0485/19/5/pdf/
i1520-0485-19-5-1288.pdf, 1989.

Walsh, E. J., Banner, M. L., Wright, C. W., Vandemark, D. C., Chapron, B., Jensen, J., and Lee, S.: The Southern Ocean Waves Experiment. Part III: sea surface slope statistics and near-nadir remote sensing, J. Phys. Oceanogr., 38, 670–685, doi:10.1175/2007JPO3771.1, 2008.

Yueh, S. H., Tang, W., Fore, A. G., Neumann, G., Hayashi, A., Freedman, A., Chaubell, J., and Lagerloef, G. S. E.: L-Band passive and
15   active microwave geophysical model functions of ocean surface winds and applications to Aquarius retrieval, IEEE Trans. on Geosci. and Remote Sensing, 51, 4619–4632, 2013.

Yurovsky, Y. Y., Kudryavtsev, V. N., Grodsky, S. A., and Chapron, B.: Sea surface Ka-band doppler measurements: analysis and model development, Remote Sensing, 11, 839, doi:10.3390/rs11070839, 2019.

Zrnic, D. S.: Spectral moments estimates from correlated pulse pairs, IEEE Trans. Aero. Electronic Sys., 13, 344–354,
20   doi:10.1109/TAES.1977.308467, 1977.